

From many-body to many-time physics

G. A. L. White,^{1,*} F. A. Pollock,² L. C. L. Hollenberg,¹ C. D. Hill,^{1,3} and K. Modi^{2,†}

¹*School of Physics, University of Melbourne, Parkville, VIC 3010, Australia*

²*School of Physics and Astronomy, Monash University, Clayton, VIC 3800, Australia*

³*School of Mathematics and Statistics, University of Melbourne, Parkville, VIC, 3010, Australia*

Multi-time quantum processes are endowed with the same richness as many-body physics, including temporal entanglement and well-defined causal structures. We dub this *many-time physics*, and show how surprisingly accessible, yet under-explored, these phenomena are in nascent quantum processors. Here, we develop a family of tools that allow us access to many-time physics on quantum information processors, which are then demonstrated. First, we access short-range microscopic properties, such as genuine multi-time entanglement and estimators for non-Markovian memory. Then, adapting classical shadow tomography to many-time scenarios, we access macroscopic features like long-range correlations and compact representations of large processes. We showcase this for a 20-step process (42-qubit state) by accurately capturing numerous facets of the dynamics, including multi-time correlations – for example, in the prediction of mid-circuit measurement distributions. Our techniques are pertinent to generic quantum stochastic dynamical processes, with a scope ranging across condensed matter physics, quantum biology, and in-depth diagnostics of NISQ era quantum devices.

Quantum correlations are at the heart of most captivating microscopic phenomena, which are linked in stronger ways than any classical system. The microscopic correlations affect the macroscopic properties of many-body quantum systems, leading to exotic phases of matter. Discourse on this topic is typically dominated by spatial correlations exhibited at a single time, or where time is merely a parameter for investigating the evolution of spatial properties [1, 2].

In contrast, comparatively little has been studied on the subject of *many-time* physics. A single quantum system may have rich dynamics, especially when it interacts with its environment. The relative sparseness of attention is in part due to the fact that it has been a challenge to put multi-time correlations on equal footing as spatial ones. Recent developments in the theory of quantum stochastic processes have closed this gap to map multi-time processes to many-body states [3–7] by means of the generalised Choi-Jamiołkowski isomorphism (CJI) [8]. It is becoming evident that many-time physics is as vibrant as many-body physics; they are endowed with nontrivial temporal entanglement [9], exotic causal properties [10–15], rich statistical structures [16], resources [17–19], and a window into novel physics [20, 21].

In this work, we address the question: how can we access the fantastic phenomena listed above? By doing so, we open the door up to the realistic observation and study of temporal correlations on much the same footing as many-body states. To achieve this goal, we combine approaches well-known in many-body physics, as well as develop new techniques uniquely tailored for observables on temporal quantum states – particularly with respect to different control paradigms.

We show that quantum computers, even in their current state, offer a timely opportunity to explore the richness of many-time physics. While these machines are too noisy to manipulate into the large entangled registers required for interesting quantum algorithms, they are riddled with complex noise [22, 23], which we can access with high fidelity controls. Thus, we show that there is scope to explore interesting physics even with relatively small devices – a single qubit probed across many times, for example, can exhibit many of the same properties as large quantum states. In this sense, highly nontrivial many-time physics can be more accessible than many-body physics for the near-term quantum processors, which opens a new rich area of investigations.

Our results are divided up into two broad regimes: *micro* and *macro* properties. This is a split as natural in many-time physics as for many-body physics. In the micro regime, restricted only to high fidelity unitary operations, followed by a final terminating measurement, we show how to witness genuine multitime entanglement, as well as devise tight bounds for various facets of non-Markovian memory. In the macro regime, we manufacture access to a range of higher-control quantum instruments (probabilistic quantum maps). This allows us to probe the process in full generality. Using established techniques such as classical shadows and matrix product operator (MPO) tomography, we show how to access properties of arbitrarily sized processes.

We then show the high efficacy of these methods by extracting features of many-time physics in a series of quantum simulations of complex dynamics on IBM Quantum processors. These vary from in-depth small scale processes, to characterisation of a 20-step process. Applications of this work range from the diagnostics of temporally correlated noise in quantum technologies [22, 24], to the observation and simulation of dynamical complexity in condensed matter systems [25–27], to quantum biology [28, 29] and quantum causal modelling [5].

* white.g@unimelb.edu.au

† kavan.modi@monash.edu

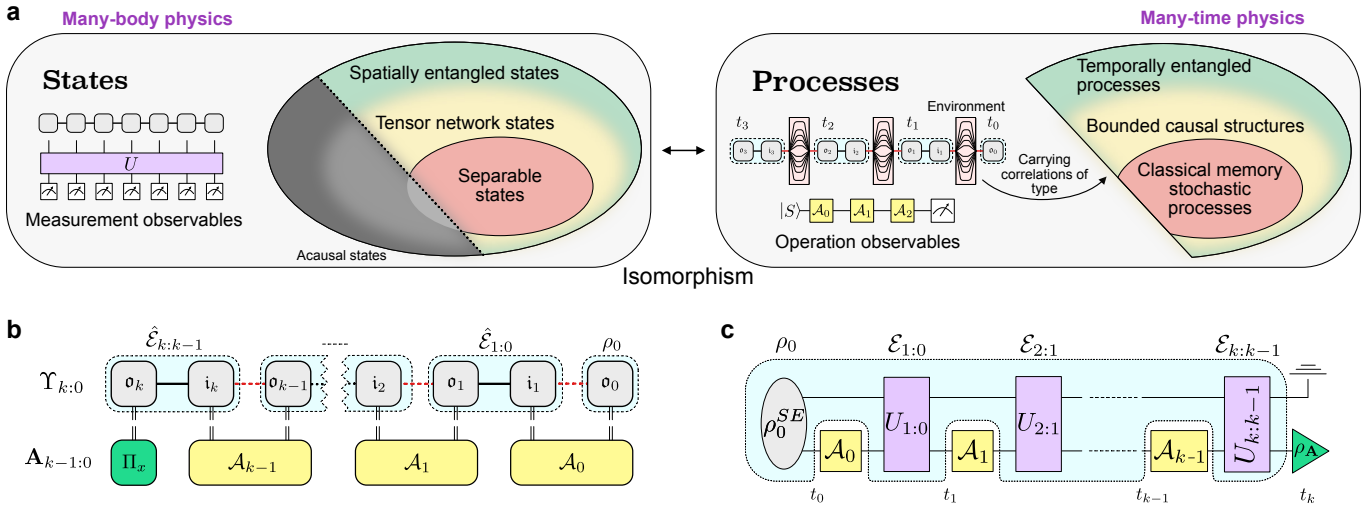


FIG. 1. **a** A depiction of the space of processes as compared to a subset of states, linked by the Choi-Jamiołkowski isomorphism. Many of the exotic features of many-body physics can be linked to processes, thus generating an equivalent many-time physics. The space of processes is not isomorphic to all states, but rather states that obey a set of causality conditions. **b** A k -step process tensor Choi state. This object represents a sequence of possibly correlated CPTP maps between different points in time, plus average initial state. Output legs o_i are mapped by a control operation \mathcal{A}_i to the next input leg i_{i+1} . **c** Circuit form of a process tensor with arbitrary SE interactions. Operations at different times map to a final state conditioned on these choices. The process tensor represents everything shaded in blue, the uncontrollable system-environment dynamics.

MULTI-TIME PROCESSES AS MANY-BODY QUANTUM STATES

The famous CJI displays an equivalency between two-time dynamical processes – like a unitary process – and a quantum state. Properties of this so-called dynamical map can be deduced from properties of the Choi state [8]. The generalisation of the CJI extends to multi-time processes by which sequences of dynamical maps can be temporally correlated. The state equivalence ensures that many of the features of many-body physics have a temporal parallel in many-time physics: observables, separable states, discord, and entanglement all have equivalent meaning in processes. We depict this in Figure 1a. The generation of temporal correlations across multiple times has a different physical origin, however. They necessarily emerge from strong interactions with a complex environment. Information can travel into a (quantum or classical) bath and return at a later point in time to interact with the system, distributing correlations [7, 30]. The properties of this non-Markovian memory depends on both the interaction and the bath coherence. Such non-Markovian quantum stochastic processes are fully describable under the process tensor framework [4, 7]. Recently, the advent of process tensor tomography (PTT) has facilitated the estimation of this object on real devices [22, 23].

In any given experiment, there is a distinction between controllable operations implemented by the experimenter on a d -dimensional system, and uncontrollable stochastic dynamics due to system-environment (SE) interactions. A quantum stochastic process accounts

for all quantum correlations across a number of times $\mathbf{T}_k := \{t_0, \dots, t_k\}$. Such processes are represented as a multilinear map from a sequences of controllable operations on the system to a final state density matrix. Here, the map, known as a process tensor [4, 5], represents all of the uncontrollable dynamics of the process, depicted as the background in Figure 1c. Through the CJI, this mapping is encapsulated by its Choi state $\Upsilon_{k:0}$ over k time steps as a correlated multipartite density operator. Its two-time marginals are completely positive, trace-preserving (CPTP) maps $\hat{\mathcal{E}}_{j+1:j}$ for each sequential pair in \mathbf{T}_k , with average initial state ρ_0 . Each marginal has an input and an output tensor leg, starting from the initial state. Collectively, we label these $\{o_k, i_k, o_{k-1}, \dots, i_1, o_0\}$ and feature an example Choi state in Figure 1b.

The operations that drive an experiment can be represented generically by a set of CP maps $\{\mathcal{A}_0, \mathcal{A}_1, \dots, \mathcal{A}_{k-1}\}$ such that the Choi state of the full sequence is given by $\mathbf{A}_{k-1:0} = \bigotimes_{i=0}^{k-1} \mathcal{A}_i$. The final output distribution, conditioned on these operations and measurement apparatus $\{\Pi_x\}$, is then given by the spatiotemporal generalisation of Born's rule [31]:

$$p_x | \mathbf{A}_{k-1:0} = \text{Tr} [\Upsilon_{k:0} (\Pi_x \otimes \mathbf{A}_{k-1:0}^T)]. \quad (1)$$

This generalises joint probability distributions of a classical stochastic process to the quantum regime [32]. The key insight to Equation (1) is that operations on a system at different points in time constitute observables on the process tensor Choi state. These may be deterministically applied – such as a unitary operation – or stochastic, such as a measurement and feed-forward or

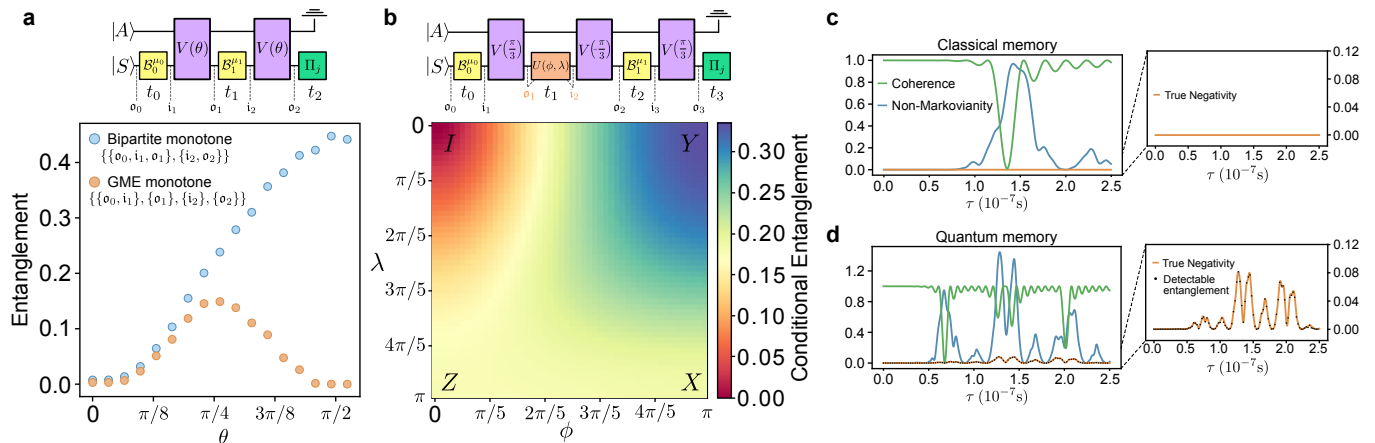


FIG. 2. Implementation of unitary-restricted temporal entanglement witnesses. **a** Results of a circuit designed to manufacture different temporal entanglement structures implemented on *ibm_cairo*. **b** We construct a three-step process tensor on *ibm_auckland* and show how deterministically changing the intermediate unitary gives control over the resulting temporal quantum correlations. **c** A classical field generates non-Markovian correlations, but entanglement in the process tensor of a simulated quantum sensor remains zero. **d** When the multi-time correlations are genuinely quantum, we show that this may be detectable by the sensor with unitary-constrained control.

more general quantum instruments. In this work, we use this perspective of temporal observables to explore the notion of many-time physics as analogous to the study of many-body state properties.

CAPTURING MICRO PROPERTIES OF MANY-TIME PHYSICS

We start with the microscopic characterisation of quantum processes. We also restrict considerations to where only sequences of unitary operations and a terminating measurement are available – i.e. a tomographically incomplete scenario consistent with most technology. From this, we show how it is possible to obtain various microscopic properties of quantum processes, including non-Markovian memory, genuine multi-time entanglement, purity, fidelity, and generalised quantum mutual information. This restriction is significant, but we show that quantum correlations between different times are measurable even with the application of deterministic unitary sequences and a single measurement in a different temporal location. In general, these attributes are hard to obtain and require a significant amount of data and their processing. Nevertheless, this permits the study of many-time physics on both quantum computers without mid-circuit measurement capabilities and, importantly, quantum sensors which may be placed in highly complex environments. For details outlining how to obtain these unitary process observables; the structures of the spaces they generate; and their partial determination of the process tensors, see Methods.

Temporal entanglement witnesses. In continuing analogy with properties of states, temporal entanglement may be identified via its process tensor Choi state

through any of the number of mechanisms in entanglement literature. However, absent a unique or complete estimate for the process tensor, it is unclear whether genuinely quantum temporal correlations can be recognised. Here, we show by construction that the data generated by sequences of unitary operations surprisingly suffice in many instances to detect both bipartite and genuinely multipartite entanglement (GME) in time. This uses the restricted entanglement witness we tailor in Methods C. We consider two situations: experiments conducted from a qubit interacting with an ancilla on a noisy quantum device, and simulations of a quantum sensor subject to a spin-bath interaction. The former demonstrates that current experimental hardware is capable of probing these many-time physics even with relatively simple control mechanisms. The latter explores novel approaches to metrology in determining the nature of an environment [33]. Note that spatial entanglement of a system with its environment is a necessary, but not sufficient condition for temporal entanglement [34].

Our first demonstration consists of temporal entanglement experimentally verified through unitaries only on the device *ibm_cairo*. With one qubit as the simulated environment, and a two-step (three time) process tensor, we tune the SE interaction between two qubits to $V(\theta) := \exp(-i\frac{\theta}{2} \sum_i P_i \otimes P_i)$, and determine both the detectable bipartite and genuinely multipartite entanglement as a function of $\theta \in [0, \pi/2]$. The start, middle, and end of these values respectively produce an identity, $\sqrt{\text{SWAP}}$, and SWAP gate. These interactions are designed to produce different temporal entanglement structures. Repeated $\sqrt{\text{SWAP}}$ gates in principle produce GME across legs $\{i_1, o_1, i_2, o_2\}$ [7]. Meanwhile SWAP s ought to produce maximal bipartite entanglement between $\hat{\mathcal{E}}_{1:0}$ and $\hat{\mathcal{E}}_{2:1}$, since i_1 to o_2 is an effective iden-

Setup	QMI (min, max)	Negativity	Purity	Fidelity
#1. System Alone	(0.298, 0.304)	(0.0179, 0.0181)	(0.8900, 0.8904)	(0.9423, 0.9427)
#2. $ +\rangle$ Nearest Neighbours (NN)	(0.363, 0.369)	(0.0255, 0.0259)	(0.7476, 0.7485)	(0.7239, 0.7244)
#3. Periodic CNOTs on NNs in $ +\rangle$	(0.348, 0.358)	(0.0240, 0.0246)	(0.7796, 0.7811)	(0.7264, 0.7272)
#4. $ 0\rangle$ NNs with QDD	(0.358, 0.373)	(0.0205, 0.0210)	(0.8592, 0.8612)	(0.8034, 0.8045)
#5. $ +\rangle$ Long-range Neighbours	(0.329, 0.339)	(0.0209, 0.0214)	(0.8594, 0.8608)	(0.9252, 0.9260)
#6. $ +\rangle$ NN, delay, $ +\rangle$ next-to-NN	(0.322, 0.329)	(0.0209, 0.0213)	(0.8534, 0.8549)	(0.9077, 0.9083)

TABLE I. Property bounds on process tensors with different background dynamics. QMI measures the non-Markovianity of the process, with conditional QMI the minimal and maximal past-future dependence for first and last steps. Negativity measures unbound temporal bipartite entanglement. Purity indicates purity of the ensemble of open system trajectories, while fidelity captures the level of noise.

tity channel – but σ_1 and i_2 are uncorrelated, hence no GME. We realise and quantify these entanglement structures using our entanglement bound which relies only on unitary sequences. Results are shown in Figure 2a, demonstrating the ability to robustly detect entangled multi-time processes on real hardware even with limited control. In addition to varying the interaction, we also show that for a fixed process, one can ‘inject’ complexity into the circuit [34]. We reconstruct a three-step process on *ibm_auckland* and project the second time onto some parametrised unitary $U(\phi, \lambda)$. Then, for varied parameter values, compute the certifiable bipartite entanglement between $\{\sigma_0, i_1, \sigma_2\}$ and $\{i_3, \sigma_3\}$ – see Figure 2b. Thus, process correlations may be greatly manipulated even at the system level.

In the second instance, we contrast a single spin coupled respectively to classical and quantum baths. Using dynamical decoupling sequences as filter functions and sweeping through various frequencies, coherence dips correspond to locks on environmental frequencies – the point at which interactions are amplified rather than suppressed. By constructing unitary-restricted process tensors within the filter, we show that quantumness of the interaction may be certified by measuring entanglement in the multi-time correlations – as outlined in Appendix B. However, this method does not distinguish between sources which are quantum, but with interactions that can be classically emulated. This procedure is entirely consistent with the capabilities of quantum sensors, and adds a different capacity to learn about the system-environment interaction through structured sequences on the system.

Bounding process properties. Determining more complex properties of the process requires detailed information about its Choi state – such as its spectrum – beyond a restricted set of observables. To this end, unitary sequences nominally do not suffice. However, we circumvent this limitation by constructing regions of plausibility and bounding process properties among these. Measuring the outcomes to sequences of unitaries naturally generates a ‘family’ of process tensors which are consistent with the incomplete data. We develop an algorithm that searches this space of plausible process tensors to find bounds over objective functions of the user’s choosing.

This solution is discussed in Methods D and Appendix C. Thus, even without a complete estimate of a multi-time process, one may answer the next best question: what range of dynamics are consistent with a limited set of observations?

We apply this framework in the interest of mapping out the quantum and classical temporal correlations present in naturally occurring noise. We constructed six three-step process tensors in different dynamical setups for a system qubit on the superconducting device *ibmq_casablanca*. These setups were designed to examine base non-Markovianity, as well as crosstalk influence. A ten-unitary basis was used, and each process tensor obtained with maximum-likelihood PTT. Fixing these observations in the model, we then searched the family of consistent process tensors for a variety of diagnostic measures.

Specifically, we consider five information-theoretic quantities: **(i)** To measure total non-Markovianity, we employ quantum relative entropy, $S(\rho||\sigma) := \text{Tr}[\rho(\log \rho - \log \sigma)]$, between $\Upsilon_{k:0}$ and the product of its marginals $\bigotimes_{j=1}^k \hat{\mathcal{E}}_{j:j-1} \otimes \rho_0$. This is a generalisation of quantum mutual information (QMI) beyond the bipartite scenario and is endowed with a clear operational meaning [35]. **(ii)** To determine whether the non-Markovianity has genuine quantum features we quantify the entanglement in the process [9, 36] by means of negativity, $\max_{\Gamma_B} \frac{1}{2}(\|\Upsilon_{k:0}^{\Gamma_B}\|_1 - 1)$, where Γ_B is the partial transpose across some bipartition [37]. **(iii)** The purity of the process, $\text{Tr}[\Upsilon_{k:0}^2]$, measures both the strength and size of non-Markovianity through the ensemble of non-Markovian trajectories. **(iv)** Finally, quantifying both Markovian and non-Markovian noise over multiple time steps, we compute the fidelity between the ideal process and the noisy process: $\text{Tr}[\Upsilon_{k:0}(\bigotimes_{j=1}^k |\Phi^+\rangle\langle\Phi^+| \otimes \rho_{\text{ideal}})]$ with $|\Phi^+\rangle = (|00\rangle + |11\rangle)/\sqrt{2}$. Our results are summarised in Table I.

Surprisingly, we find these bounds to be extremely tight. This appears to be due to the relative purity of the process, with ranks (to numerical threshold of 10^{-8}) of between 44 and 68 for the 128×128 matrix MLE estimates, which can limit the object’s free parameters [38].

Process rank is also directly related to the size of en-

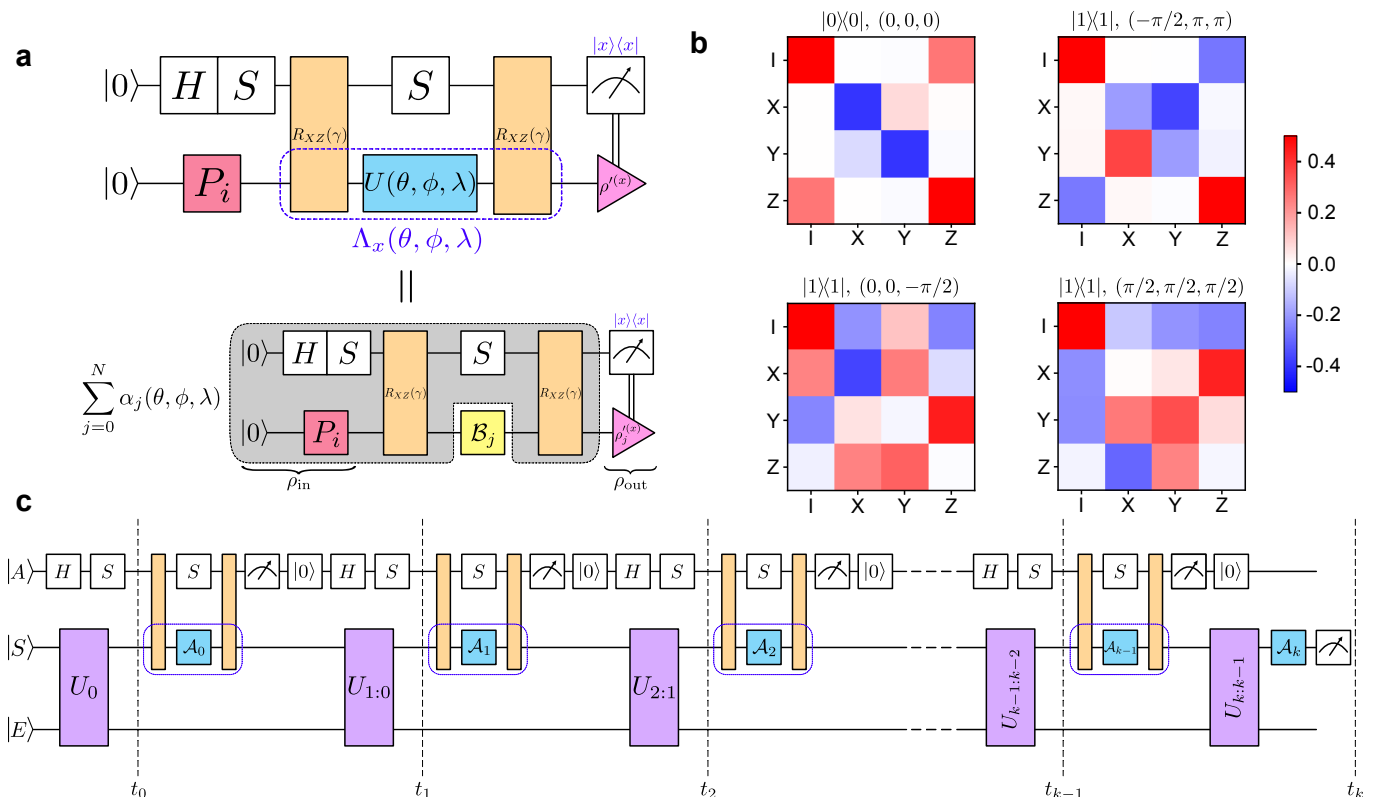


FIG. 3. Instrument design for complete multi-time statistics. **a** Using a structured system-ancilla interaction, we construct a restricted process tensor with local unitaries to realise the desired mapping. This gives an exact characterisation of the effective instrument $\Lambda_x(\theta, \phi, \lambda)$ for any choice of parameter values. **b** Some sample basis instruments implemented using this method on *ibm_perth* written in the Pauli basis, showing IC controllability including non-unital and trace-decreasing directions. **c** Many-time physics is then studied using the circuit structured as shown. The different instruments applied capture temporal quantum correlations from an arbitrarily strong *SE* interaction.

vironment, with each nontrivial eigenvector constituting a relevant bath degree of freedom. In practice, then, this both compresses requirements and estimates the effective dimension of the non-Markovian bath.

Interestingly, QMI is much larger than zero in all situations. Moreover, from the negativity across \mathbf{i}_2 and \mathbf{o}_1 we find temporal entanglement in all cases. Thus, not only are these noisy stochastic processes non-Markovian, they are bipartite quantum entangled in time. This includes Experiment #1, suggesting non-Markovian behaviour is prominent beyond even the immediate effects of crosstalk. Crosstalk certainly increases correlation strength, as well as decreasing process fidelity – an effect shown by switching neighbours into the $|+\rangle$ state and coupling to *ZZ* noise – but *ZZ* noise alone cannot generate temporal entanglement [7]. We remark that when a quadratic dynamical decoupling (QDD) protocol [39] is performed on neighbouring qubits in Experiment #4, QMI increases with respect to the other experiments, but with reasonably high fidelity. This may suggest that naive QDD reduces noise strength while increasing complexity, warranting further studies.

Although this procedure is in principle to bound generic processes, in practice, we find near complete de-

termination for only relatively few numbers of measurements. An IC three-step process tensor requires 12 288 circuits, but with only unitary gates this is 3000, so the savings are substantial. To limit experimental overhead, one might consider increasingly measuring basis sequences until bounds achieved were satisfactorily tight. This supplements, for example, machine learning approaches to directly estimate the memory [40, 41] or full characterisations [42].

CAPTURING MACRO PROPERTIES OF MANY-TIME PHYSICS

We move now onto the study of much larger processes, coarser observations, and behaviour of marginals of a process. These fit under the broad umbrella of macroscopic process properties, and can tell us, for example, how microscopic properties change as a function of time-step. Given the concerted effort to simulate correlated quantum processes classically [43–45], this connection lays the groundwork for fully general quantum simulation of non-Markovian open quantum systems. As well as simulating the dynamics (system as a function of time), a quantum

computer may also access the dynamical multi-time correlations, which encapsulates every extractable piece of information from the system.

Given the scale-up in approach, the tools developed to bound restricted processes are no longer feasible here. Instead, we require an IC basis of quantum instruments. This is achievable by interacting the system with ancilla qubits, and projectively measuring. With mid-circuit measurement capabilities, only a single ancilla is required – to be measured and reused within the circuit. Otherwise, one ancilla per time-step is necessary, and will need to be isolated post-interaction through e.g. dynamical decoupling. In this work, we perform experiments on devices with mid-circuit measurement capabilities. Note that the choice to use an ancilla is because these measurements typically have a long duration (1-5 μ s). Deferring to an ancilla allows the system to continue participating in dynamics – otherwise the window is lost if measuring the system directly. We schematically depict how we can construct and characterise a highly controllable basis of instruments from a constant number of measurements in Figure 3a, and expanded on in Methods E and Appendix E. Importantly, the effective instrument is known for any choice of local unitary on the system, without extra characterisation. Some tomographic samples of these maps as constructed on *ibm_perth* are shown in Figure 3b. The overall process is then reconstructed through circuits structured as in Figure 3c.

We are primarily motivated by the question of efficient estimation of process marginals. A key difference to the state case is the presence of both input legs in addition to the output legs. This means that measuring and forgetting is not sufficient to apply a partial trace; instead, we require application of a maximally depolarising channel. This may be physically implemented in a number of ways, but requires greater resources and would, we anticipate, be unreliable. For this reason, the method of classical shadows [46] is appealing: by randomising our instruments and post-processing the data, we can simultaneously obtain all marginals of the process and partial trace over the remainder in software. As well as circumventing a physical partial trace, this requires exponentially fewer experiments than directly computing the marginals. This requires the application of randomised sequences of local unitaries in the structure of Figure 3c, but the extension of the shadow formalism to process tensors and to quantum instruments requires slightly different post-processing which we detail in Methods F.

Estimating temporally correlated noise. The method of classical shadows permits the determination of k -point correlation functions. Translating this to processes, we examine two questions: (i) what is the average case probability of temporally correlated Pauli noise at different times?, and (ii) given the application of some operation at an earlier time, how do the dynamics of the system change at a later point? Although progress has been made with respect to these questions [47], the estimates here are with respect to the complete background

process, rather than Clifford circuits, and arbitrary temporally correlated noise as well as the special case of correlated Pauli channels. The former gives a coarse view on temporal correlations, but is an important benchmark for the feasibility of quantum error correction. The latter is a fuller diagnosis, indicating the behaviour of the device, the complexity and nature of the noise, and may be used for a more sophisticated form of quantum error mitigation, such as probabilistic error cancellation.

On the device *ibm_perth*, we apply randomised instruments using our complete basis (Fig. 3b) to characterise an idle process with random $SU(4)$ gates on neighbouring qubits. Across a seven step process, we compute the correlated dynamical maps from $t_i \rightarrow t_{i+1}$ and $t_j \rightarrow t_{j+1}$. These are given by

$$\hat{\mathcal{E}}_{j+1:j;i+1:i} := \text{Tr}_{\bar{i},\bar{j}}[\Upsilon_{k:0}], \quad (2)$$

where \bar{i}, \bar{j} indicates the trace over all process tensor legs except for $\{i_i, \sigma_i, i_j, \sigma_j\}$. From these estimates, we compute some representative components of the noise. Specifically, Figure 4b displays the negativity between each pair of maps; the trace distance between the correlated pairs and tensor product of marginals; and overlap of these maps with Pauli error channels. Some of the results are consistent with device expectations, such as e.g. the prominence of correlated Z errors compared to the other Paulis. Given that the values of these overlap terms is not commensurate with the total non-Markovianity, however, this suggests that correlated Pauli error models are not yet a good total description of the noise on current devices.

Reconstructing engineered non-Markovian processes. We conclude with a demonstration that consolidates our tools and reconstructs a long non-Markovian process simulated on a quantum device. This not only establishes that scalable non-Markovian characterisation is achievable, but presents a new aspect to simulation capabilities of quantum computers. Specifically, we consider one end of a Heisenberg-coupled spin-chain and estimate the 20-step/42-body MPO process representation from its contiguous three-step marginals (see Methods G). In each step, an $XX + YY + ZZ$ rotation is applied between each pair of neighbouring qubits in a chain of 4 (plus one acting as ancilla) on *ibm_lagos*, with each coupling chosen randomly – in total, we use 4.4×10^7 shots. The effective dimension of the environment can be compressed into numerically significant bonds between each time-step [45]. If this effective degree can be upper bounded, then the representation (and hence characterisation) can be efficient. By contracting this estimate with a sequence of instruments, we can generate a predicted probability distribution for time-series data – the 21 measurements across the circuit – illustrated in Figure 4a.

To validate that the estimate does indeed accurately capture environmental dynamics, 170 different sequences of random instruments are then run on the device at 16 384 shots. The outcomes of the instruments across the 21 different times are collected and used to generate

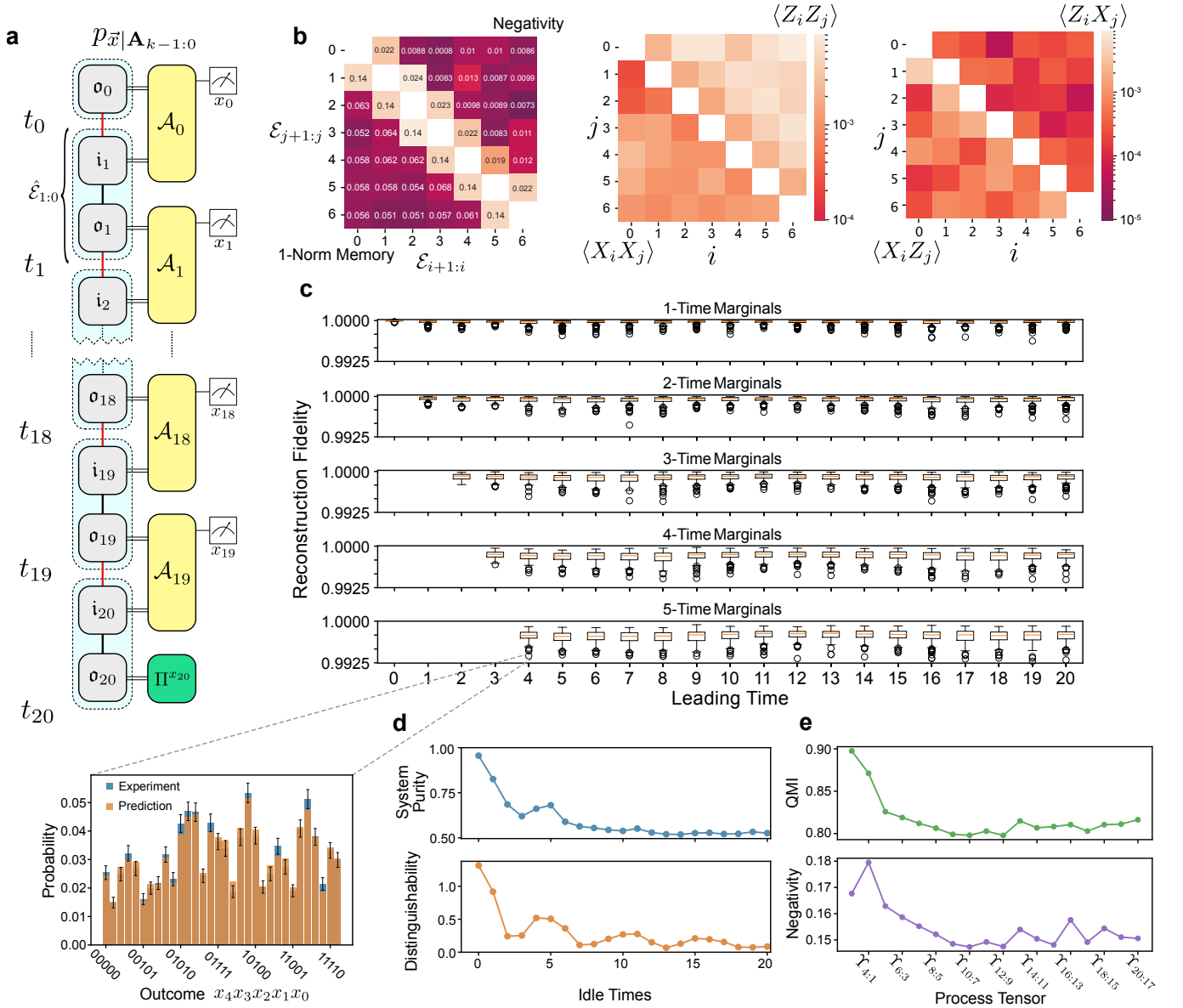


FIG. 4. Summary of macro characterisations of processes. **a** From the four-body (two-map) marginals of the a system enduring naturally idle dynamics on *ibm_perth*, we compute both the negativity between the two steps and the trace-distance between the maps and the product of their marginals. **b** We compute overlaps of the maps with correlated Pauli error channels at different points in time, allowing for a joint probability distribution to be constructed. **c** We characterise a 20-step process of a non-Markovian quantum environment on *ibm_lagos* and construct its MPO representation. This characterisation is then validated against 170 sequences of random instruments: the reconstructed process tensor is used to predict different l -time marginal probability distributions of the instrument outcomes and compared against the experimental results. **d** Properties of the system when left idle as a function of time step, showcasing conventional measures of non-Markovianity. We observe the non-monotonic behaviour of both the purity of the system, and the trace distance between two states initialised as Z and Y eigenstates. **e** Properties of the 3-step marginal process tensors as a function of time, we measure both the total memory and the temporal quantum entanglement, demonstrating a genuinely complex non-Markovian process.

different marginal probability distributions. The effect of marginalising over the outcomes at a given time is that the operation applied is a deterministic CPTP channel. The marginal probability distributions for each sequence of operations is predicted by our process characterisation and compared via Hellinger fidelity to the actual results. Figure 4c summarises the distributions of these results

for up to 5-time marginals across all 21 times, showcasing the ability to predict arbitrary components of the stochastic process to high accuracy. The computation of reconstruction statistics and comparison of our model is discussed further in Methods H.

In Figures 4d and 4e we examine the non-Markovian properties of the process from different perspectives. Fig-

ure 4d looks at conventional non-Markovian flags in oscillations of the system’s purity, and the distinguishability of two states as a function of time. Meanwhile Figure 4e conveys exact measures of non-Markovianity throughout the process. We see that both the generalised QMI, and negativity across the middle cut of the three-step process marginals both decay to a non-zero constant value. Despite the nominal decay of the system, memory effects persist in the dynamics, as can be detected through mid-circuit measurements. Moreover, this memory is genuinely complex, but not so large that our MPO model is unable to capture the necessary degrees of freedom.

Here, we have gone beyond the state-of-the-art in characterising quantum stochastic processes. We have shown how one may completely characterise arbitrarily many time-steps in a quantum process by using the available hardware to manufacture full system control. Further, through our demonstration we validate the ability to predict the statistics produced by arbitrary sequences of instruments with mid-circuit measurements. This broadens the study of processes to a far more macro level, widening the scope to more intricate considerations such as thermalisation and equilibration.

DISCUSSION

Although the study of many-body physics has uncovered a rich tapestry of structure in different corners of applied quantum mechanics, temporal quantum correlations remain relatively under-explored. In this work, we have motivated, demonstrated, and made accessible the study of many-time physics beyond the two-time correlators regime. Multi-time correlations will showcase the full potential of the field of many-time physics, including capturing dynamical phases of matter [48].

A primary achievement is in showing how rich non-Markovian effects can be studied with only unitary control and a final projective measurement. Rather than merely simulating non-Markovian quantum processes on fully controllable quantum computers, this allows observation of complex naturally occurring phenomena [28, 49–53]. One might imagine, for example, the use of quantum sensors in condensed matter or biological systems. Nitrogen-vacancy centres in diamond, for example, can be unitarily controlled with arbitrary waveform generators, projectively read out optically, and have been shown to be biocompatible [29].

Our results on IBM Quantum devices show that even idle qubits can exhibit surprisingly complex and temporally correlated dynamics. This prompts the need for further study of non-Markovian behaviour on NISQ devices. Specifically, if not fabricated away, correlated noise ought to be able to be converted into clean channels through appropriate control sequences [18].

Finally, given the use of ancilla qubits, we have also shown how to arbitrarily capture many-time physics through repeated probes of a system. This naturally fits

into models of quantum simulation, but provides strictly more information than simply observing evolution of a state. From this, we can envisage the transduction of multi-time observables from a single non-Markovian quantum system into (classical or quantum) machine learning algorithms, which has recently been shown as a promising avenue for quantum advantage [54].

METHODS

A. Process tensor tomography

All restricted and unrestricted process tensors in this work are estimated using maximum-likelihood estimation (MLE) PTT, as described in Ref. [23]. We briefly outline this method here.

All process tensors have a density matrix representation, $\Upsilon_{k:0}$, from which one can make predictions through the generalised version of Born’s rule. Specifically, for a sequence of $k - 1$ (possibly stochastic) quantum operations $\{\mathcal{B}_j^{\mu_j}\}$, and a final measurement $\{\Pi_i\}$, the predicted outcome probability is

$$p_{i,\vec{\mu}} = \text{Tr} \left[(\Pi_i \otimes \mathcal{B}_{k-1}^{\mu_{k-1}\text{T}} \otimes \cdots \otimes \mathcal{B}_0^{\mu_0\text{T}}) \Upsilon_{k:0} \right]. \quad (3)$$

If the $p_{i,\vec{\mu}}$ are known for an informationally complete $\{\Pi_i\}$ and $\{\mathcal{B}_j^{\mu_j}\}$, then the set of linear equations uniquely fixes $\Upsilon_{k:0}$. Alternatively, if they are known for some subspace of operations (in this work, we are frequently restricted to the space of unitary operations), then the process tensor will be uniquely fixed on that subspace. However, in reality, the measured outcomes $n_{i,\vec{\mu}}$ are noisy estimates of the ‘true’ probabilities, and there is often no physical process tensor that completely matches the data. For this reason – as is common – we treat estimation of a process as an optimisation problem where a model for the process is fit to the data. Specifically, a unique $\Upsilon_{k:0}$ is found by minimising the log-likelihood

$$f(\Upsilon_{k:0}) = \sum_{i,\vec{\mu}} -n_{i,\vec{\mu}} \ln p_{i,\vec{\mu}}, \quad (4)$$

where $\Upsilon_{k:0}$ is a positive matrix obeying a set of causality conditions. This optimisation is carried out using a projected gradient descent algorithm, where at each step the model is iterated in a direction that decreases the log-likelihood, but always constrained to lie on the manifold of positive, causal states. More details can be found in Ref. [23].

B. Restricted many-time observables

Rigorous characterisation of non-Markovianity necessarily requires measurement and feed-forward capabilities. This is because temporal correlations due to the environment must be separated out from correlations at

the system level with the use of causal breaks. Given that many engineered and naturally occurring systems can only be manipulated with fast unitary operations followed by a projective measurement, it is necessary to consider what exactly can be inferred about the non-Markovianity given this limitation. We investigate this situation here. With unitary-limited control, the measurement apparatus for probing a process tensor is not tomographically complete. We first explore what this means explicitly, and subsequently determine what can still be inferred about the process from limited data. Consider a process tensor with decomposition $\Upsilon_{k:0} = \Upsilon_{k:0}^{(R)} + \Upsilon_{k:0}^{(R_\perp)}$, where $\Upsilon_{k:0}^{(R)}$ is fixed by a restricted set of experimental observations, and $\Upsilon_{k:0}^{(R_\perp)}$ its free (modulo physical constraints) orthogonal complement.

In the CJI picture, unitaries are maximally entangled. Thus, there are $d^4 - 2d^2 + 2$ nontrivial Pauli terms – the weight-2 operators and $\langle \mathbb{I} \rangle$. Equation (1) shows how the action of a process tensor constitutes projecting its Choi state onto the Choi state of the sequence. Correspondingly, the operation \mathcal{A}_l evaluates expectation values with respect to indices i_{l+1} and o_l . The nontrivial Pauli expectations partition into non-unital $\langle P_n \mathbb{I} \rangle$, trace-decreasing $\langle \mathbb{I} P_m \rangle$, and unitary $\langle P_n P_m \rangle$ maps, which each overlap with either marginals or correlation terms. Thus, when restricted only to unitary operations on a single qubit, the observables \mathcal{O} on $\Upsilon_{k:0}$ which we have access to are limited to properties of $\Upsilon_{k:0}^{(R)}$ and take the form

$$\mathcal{O} = \sum_{i, \bar{\mu}} \alpha_{i, \bar{\mu}} P_i \otimes \bigotimes_{j=0}^k P_{\mu_j}, \quad \text{where} \quad (5)$$

$$\alpha_{i, \bar{\mu}} \in \mathbb{R},$$

$$P_i \in \{\mathbb{I}, X, Y, Z\},$$

$$P_{\mu_j} \in \{\mathbb{I}\} \cup \{X, Y, Z\} \otimes \{X, Y, Z\}.$$

Collecting only this data induces a ‘family’ of process tensors, defined as the set of process tensors whose restriction to this subspace is equal – see Figure 5a. We will denote the subspace of observables of the form of Equation (5) by \mathfrak{U} .

C. Unitary witnesses for temporal quantum entanglement

Where measurements at different times are possible, temporal entanglement seems much like spatial entanglement: measurements on different subsystems are more strongly correlated than can be explained by any classical cause. Where the connection is less obvious, however, is where input legs are included and only unitary control is applied at different times followed by a final terminating measurement. This question is of keen relevance in the NISQ era – how much information can be extracted about temporal correlations without the technology to perform high fidelity causal breaks? Here, we add to at

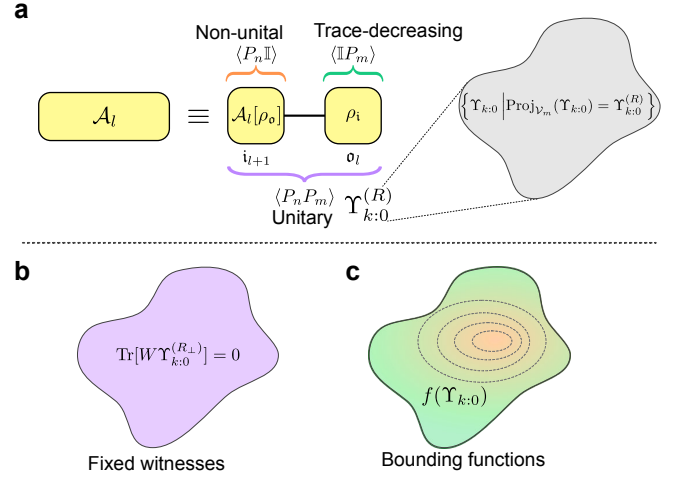


FIG. 5. Property determination from restricted process tensors. **a** Observable interventions naturally partition into non-unital, trace-decreasing, and unitary controls. Unitary-only characterisation generates a family of process tensors consistent with this limited data. **b** Temporal entanglement may be certified by finding entanglement witnesses whose value is determined only by the observed data. **c** More informative functions of the process may be bounded by finding extrema across the process tensor family.

least one facet of the discussion by showing a somewhat remarkable fact to the affirmative: that temporal entanglement can indeed be both detected and measured with only unitary operations followed by a terminating measurement.

We show this by construction, using the entanglement witness of Ref. [55] and constraining it to lie within the span of unitary operations. This witness is found by means of a semidefinite program (SDP), solving the optimisation problem

$$\min_{W \in \mathfrak{W}} \text{Tr}[W \Upsilon_{k:0}],$$

$$\mathfrak{W} = \{W | \forall M : \exists P_M, Q_M \succcurlyeq 0 : W = P_M + Q_M^{\Gamma_M}, \quad (6)$$

$$\text{Tr}[W] = 1, W \in \mathfrak{U}\}.$$

Here, M denotes a partition of the subsystems of $\Upsilon_{k:0}$, and Γ_M is the partial transpose with respect to that partition. The set of all available partitions will depend on the target of the entanglement witness – i.e. an n -partite entanglement witness will cover 2^{n-1} unique partitions. If W is found such that $\text{Tr}[W \Upsilon_{k:0}] < 0$ then $\Upsilon_{k:0}$ is genuinely multipartite entangled across the defined partitions. By replacing condition $\text{Tr}[W] = 1$ with $P_M, Q_M \preccurlyeq \mathbb{I}$ then the resulting minimisation defines a lower bound entanglement monotone, which we employ. In the bipartite case, this lower bounds the negativity.

When a process tensor $\Upsilon_{k:0}$ is estimated from restricted experimental data, a non-unique Choi state is constructed obeying conditions of complete positivity and causality. But so long as $W \in \mathfrak{U}$ is imposed, the

witness is restricted to be an observable on $\Upsilon_{k:0}^{(R)}$ which is uniquely fixed (Figure 5b). Thus, we may solve the SDP given in Equation (6) to detect both bipartite and multipartite entanglement in time, even with extremely simple circuits such as sequences of unitary operations. Although this witness is not as powerful as a fully generic observable on $\Upsilon_{k:0}$, we find it sufficient to detect temporal entanglement in practice. This result extends the boundaries of what can be determined about the dynamics of an open quantum system, and should in particular find utility in the study of naturally occurring quantum stochastic processes.

Entanglement structures may be witnessed in fixed processes, but we also explore how they can be controlled. Applying a fixed operation on the system physically transforms one process into a new one. This new process can be taken to be the old process, where one step is projected onto the fixed operation. In our example of controllable entanglement in the main text (Figure 2b), we first estimate a three-step process tensor $\Upsilon_{3:0}$. A conditional two-step marginal is then found for parametrised unitary

$$V(\phi, \lambda) = \begin{pmatrix} \cos(\phi/2) & -e^{i\lambda} \sin(\phi/2) \\ \sin(\theta/2) & e^{i\lambda} \cos(\phi/2) \end{pmatrix} \quad (7)$$

Let $\mathcal{V}(\phi, \lambda)$ be the Choi state of $V(\phi, \lambda)$, then

$$\Upsilon_{2:0}^{(\mathcal{V}(\phi, \lambda))} = \text{Tr}_{i_2, o_1} [(\mathbb{I}_{o_3, i_3, o_2} \otimes \mathcal{V}(\phi, \lambda)^T \otimes \mathbb{I}_{i_1, o_0}) \cdot \Upsilon_{3:0}], \quad (8)$$

which is the two-step conditional marginal process where $V(\phi, \lambda)$ is applied in position 1 of the circuit. For $\phi \in [0, \pi]$ and $\lambda \in [0, \pi]$ we compute the unitary entanglement lower bound Equation (6) between legs $\{o_0, i_1\}$ and $\{o_2, i_3, o_3\}$. This determines how much complex temporal correlations can be produced or modified by user-chosen controls.

D. Bounding properties of the full process

When Equation (1) is measured experimentally for a quorum, $\mathcal{O}(d^{4k})$, of control sequences, the process tensor is uniquely fixed and one can straightforwardly quantify the non-Markovian correlations [42].

Our aim is to infer a full process and quantify non-Markovian correlation therein from given limited data. The space of k -step process tensors is given through the CJI by the set of $2k+1$ -partite density matrices satisfying causality conditions. Specifically, they are unit-trace positive matrices satisfying

$$\text{Tr}_{o_j} [\Upsilon_{j:0}] = \mathbb{I}_{i_j} \otimes \Upsilon_{j-1:0} \quad (9)$$

for each j . Physically, causality conditions ensure that averaging over future operations does not affect the statistics of the past. Mathematically, they generate a hyperplane of dimension $\sum_{j=1}^k (d^2 - 1)d^{4j-2}$ plus one for normalisation [23]. We denote this affine space \mathcal{V}_c .

In Ref. [23], we developed a projection routine as part of maximum likelihood estimation (MLE) to impose $\Upsilon_{k:0} \in \mathcal{S}_n^+ \cap \mathcal{V}_c$. We extend this in two ways here: first, we expand the affine space to include observed data, and second, we consider a range of different information-theoretic quantities as our objective to find maxima and minima. This opens up exploration of process tensor families consistent with the limited observations. The technique functions generically, however for concreteness we consider the restriction of unitary-only control sequences followed by a terminating measurement, as in Figure 5a.

Now, suppose we have probed a process solely without an IC basis. Then, after treating the data with MLE, we have a set of observations $p_{i, \vec{\mu}}$ corresponding to our restricted basis $\mathfrak{B} := \{\mathbf{B}_{k-1:0}^{\vec{\mu}}\} := \{\otimes_{j=0}^{k-1} \mathcal{B}_j^{\mu_j}\}$ and POVM $\mathcal{J} := \{\Pi_i\}$. We can construct a new affine space \mathcal{V}_m from these observations, given by

$$\left\{ \Upsilon_{k:0} \in \mathbb{C}^{n \times n} \mid \text{Tr} \left[\Upsilon_{k:0} \left(\Pi_i \otimes \mathbf{B}_{k-1:0}^{\vec{\mu}T} \right) \right] = p_{i, \vec{\mu}} \right\} \quad (10)$$

$$\forall \Pi_i \in \mathcal{J}, \mathbf{B}_{k-1:0}^{\vec{\mu}} \in \mathfrak{B}.$$

Consequently, the family of process tensors which are consistent with our observations is given by the intersection of the cone \mathcal{S}_n^+ and the affine space $\mathcal{V} := \mathcal{V}_c \oplus \mathcal{V}_m$ (Figure 1b). As in Ref. [23], we optimise some objective function over the feasible set using the pgdb algorithm [23, 56]. In short, we perform gradient descent with a chosen function, where at each iteration the object is projected onto $\mathcal{S}_n^+ \cap \mathcal{V}$. Using this technique we find minimum and maximum bounds for the values that any differentiable function can take for all process tensors consistent with observed data.

E. Bootstrapped construction of quantum instruments

The tools to probe process tensors are most completely described by quantum instruments – stochastic maps with a post-measurement state. We show here how restricted process tensors can manipulate an interaction with an ancilla qubit, creating an arbitrary well-characterised effective map. These maps can then be used to probe SE dynamics with a full process tensor; hence, ‘bootstrapped’.

A quantum instrument $\{\mathcal{A}_x\}_{x \in \mathcal{X}}$ is a set of completely positive, trace-non-increasing (CPTNI) maps, indexed by a finite alphabet \mathcal{X} such that the sum map $\sum_{x \in \mathcal{X}} \mathcal{A}_x$ is a CPTP map. The output of the instrument can be defined as a classical-quantum channel:

$$\mathcal{A}(\rho) = \sum_{x \in \mathcal{X}} |x\rangle\langle x|_A \otimes \mathcal{A}_x(\rho), \quad (11)$$

where a classical register stores the output of some projective measurement on an ancilla register. A CPTP map then is ignorant about the outcomes of these measurements, whereas CPTNI maps are non-deterministic operations that can be implemented by bookkeeping the

measured states on the system, conditional on the measurement outcomes of the ancillae. They thus fully describe measurements made on a system as well as a post-measurement state [57].

Importantly, in a real setting, the instruments used for characterisation must be both fast and *known*. We introduce here a practical procedure to accomplish both. By driving a cross-resonance interaction [58] between the system and its ancilla and measuring, we engineer a short non-Markovian interaction from the system perspective. We construct a restricted process tensor around the SA interaction which maps from local S unitaries to the final classical-quantum state given by the projective measurement on A and QST on S . The ideal circuit structure is given in Figure 3. Note however, that there are likely to be extraneous local terms introduced by these cross-resonance interactions, so we cannot necessarily rely on them as pure ZX interactions. The resulting object is a quantum instrument on S .

Given that we would like to be able to apply any local unitary $U(\theta, \phi, \lambda)$ and know the effective map $\mathcal{A}_x(\theta, \phi, \lambda)$ from the SA interaction, we first construct a restricted process tensor which maps from the local unitary to output, as shown in Figure 3a.

Employing Equation (1), the experimentally reconstructed process tensor can determine the exact output subject to an arbitrary local gate. The conditional map realises a Stinespring dilation, while circumventing any possible errors that occurred in generating the operation. Thus, we have a quantum instrument fully parametrised in terms of our local unitary on S . This allows us to classically find the set of parameters which lead to a desirable set of quantum instruments – Figure 3b shows some representative basis instruments from applying this procedure on *ibm.perth*. Because this method requires manipulation of a system with initial correlations, this procedure would be otherwise not possible without employing using of a process tensor to bootstrap the construction. For full details on the basis and its implementation, see Appendix E. Since these instruments then permit us complete control of the system, we can use them for complete process characterisation as illustrated in Figure 3c.

F. Classical shadows across multi-time processes

Recent seminal work from Huang et al. has introduced the powerful concept of classical shadows: a procedure of randomised measurements and post-processing to estimate M quantum state observables in $\log M$ measurements, with extra scaling factors that depend on properties of the observable as well as the randomisation procedure [46]. This has recently been extended to quantum process tomography, and in the estimation of gate set properties [59, 60]. Here, we show the natural application of this to multi-time processes, including discussion of causally-imposed idiosyncrasies. We first look to temporal correlation functions and then efficient representa-

tions of the entire process.

Classical shadow tomography is more restrictive in the process case than the state case, since process causality conditions – of the form of Equation (9) – restrict the types of correlations that can exist. The identity matrix Choi state is equivalent to averaging over a full set of instruments, or replacing the system with a maximally mixed state. From here, the only temporal correlations that persist are thus non-unital ones. i.e. the environment must unmix the system in a way that depends on the instrument applied to the system at a previous time. Although classical shadows will be useful for correlations of this form, it is a particularly restrictive class of non-Markovianity.

Given a basis of operations at the i th time $\{\hat{\mathcal{B}}_i^{\mu_i}\}$ with Choi states $\{\hat{\mathcal{B}}_i^{\mu_i}\}$, there exists a *dual* set $\mathcal{D} := \{\Delta_j^{\mu_j}\}$ such that the process tensor may be written [61]

$$\Upsilon_{k:0} = \sum_{i, \vec{\mu}} p_k^{i, \vec{\mu}} \omega_i \otimes \Delta_{k-1}^{\mu_{k-1} \text{ T}} \otimes \dots \otimes \Delta_1^{\mu_1 \text{ T}} \otimes \Delta_0^{\mu_0 \text{ T}}. \quad (12)$$

When a linearly independent basis is chosen, the duals satisfy $\text{Tr}[\hat{\mathcal{B}}_i \Delta_j] = \delta_{ij}$. Similarly, we have expanded the final state $\rho_k^{\vec{\mu}}$ in terms of the dual operators ω_i of the proving POVM $\{\Pi_i\}$, i.e., $\rho_k^{\vec{\mu}} = \sum_i p_k^{i, \vec{\mu}} \omega_i$. Here, $p^{i, \vec{\mu}}$ is the probability of the detector clicking with outcome i subject to some sequence of operations $\mathbf{B}_{k-1:0}^{\vec{\mu}}$. Another way to say this is that Equation (12) is the linear inversion estimate of $\Upsilon_{k:0}$. As a consequence, the single-shot version of Equation (12) is exactly a classical shadow.

To compute the shadows from a sequence of instruments, first, let N be the size of the (possibly under or overcomplete) basis. We can write each of the Choi $\hat{\mathcal{B}}_i^{\mu_i}$ as a row vector (adopting a row-vectorised convention) $\langle\langle \hat{\mathcal{B}}_i^{\mu_i} |$ and from this construct a single matrix \mathcal{M}_i :

$$\mathcal{M}_i = \begin{pmatrix} \langle\langle \hat{\mathcal{B}}_i^0 | \\ \langle\langle \hat{\mathcal{B}}_i^1 | \\ \vdots \\ \langle\langle \hat{\mathcal{B}}_i^{N-1} | \end{pmatrix}. \quad (13)$$

Now, the matrix $\mathcal{M}_i^{\dagger\dagger}$ (right-inverse, conjugate transposed) contains the dual matrices $\{\Delta_i^{\mu_i}\}$ to $\{\hat{\mathcal{B}}_i^{\mu_i}\}$ in its rows, which are then trace normalised.

In practice, we use the parametrised set of instruments described briefly in the previous subsection, and in more depth in Appendix E. Our basis set consists of the instruments generated by a local Clifford gate on the system, plus the projective measurement outcome on the ancilla for a total of 48 different basis elements. For each randomised sequence, a sequence of Cliffords are applied to the system (recalling that these are each sandwiched between fixed SA interactions), and the outcome of the series of mid-circuit measurements on the ancilla qubit recorded, $x_k x_{k-1} \dots x_0$. The duals to this basis of 48 instruments are computed, and the classical shadow of the process tensor represented as

$$\hat{\Upsilon}_{k:0}^{\vec{x}, \vec{\mu}} := \omega_{x_k} \otimes \Delta_{k-1}^{\mu_{k-1}(x_{k-1})\text{T}} \otimes \dots \otimes \Delta_1^{\mu_1(x_1)\text{T}} \otimes \Delta_0^{\mu_0(x_0)\text{T}}. \quad (14)$$

This provides a computationally convenient method to compute the classical shadow for an arbitrary ensemble of quantum instruments, with efficient computation of observables as per the classical shadow routine. As proved in Ref. [46], collecting, collecting $\log M$ suffices to estimate M linear functions of $\Upsilon_{k:0}$, with extra scaling factors in the locality of the observable. Our key motivation for bringing shadows to the temporal domain is that it allows us to perform a partial trace in software by averaging over all instruments, and allows us to collect all the k -time marginals of a process with only logarithmically many more circuits. In direct analogy to the state case, we may compute linear functions of the process tensor by using the median-of-means algorithm given in [46]. From this, we can estimate the required many-time observables that uniquely fix a process tensor (e.g. the 4^{2k+1} Pauli terms), and perform MLE PTT to estimate the process tensor marginals.

G. Reconstructing temporal matrix product operators

Given the ability to represent a process tensor as a density matrix, it is perhaps unsurprising that the mapping has a well-established matrix product operator (MPO) representation [4, 40, 45, 62]. Using efficient characterisation techniques coupled with the classical shadows method, we leverage this structure here to present a method by which the non-Markovian dynamics of a system may be reconstructed as a temporal MPO. Among applications of studying natural dynamics of quantum systems, we envisage the simulation of more complex dynamics (such as the archetypal spin-boson model) to be accomplished in this way. This topology is particularly desirable for process tensors, since casual ordering ensures the object is strictly one-dimensional. The process tensor MPO comprises each local subsystem $\{\sigma_0, i_1, \dots, i_k, \sigma_k\}$ – the input and output legs to the process at each time. The bond dimension between channels (grouped by σ_l and i_l) constitutes a measure of non-Markovianity. Moreover, this efficient representation allows us to learn more about the multi-time statistics than would otherwise be possible with a complete representation.

In Ref. [63] it was shown that a 1D state could be reconstructed from reduced states on an odd number R neighbouring spins of dimension d , so long as the MPO maximum bond dimension did not exceed d^{R-1} . We briefly summarise the procedure, and outline its application in the context of process tensors. As an ansatz, a left and a right rank (d^{2l}, d^{2r} respectively) are chosen for an n -body state. The marginals for this state will then be R -body, where $R = l + r + 1$ – giving $n - R + 1$ local marginals. In a process tensor context, we have k steps,

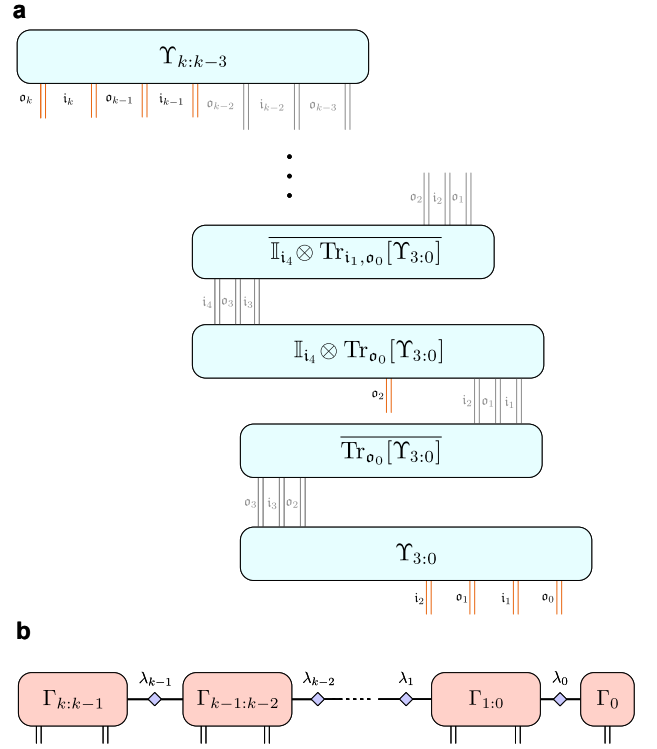


FIG. 6. Reconstruction of a temporal MPO. **a** We construct the process tensor as a temporal MPO by stitching together ℓ step marginals estimated from classical shadows. Here is an example taking $\ell = 3$. Note that the overline denotes a pseudoinverse of the matrix. Orange legs are free indices, and grey legs are contracted indices which are the MPO bonds. **b** The resulting MPO representation after condensing down the above (and appropriately splitting sites at the start and finish). The bond dimension (if smaller than the rank of the marginals) corresponds to the size of the non-Markovian memory.

or a $2k + 1$ -body state. If $l = r := \ell$, then the problem requires estimation of all ℓ step marginals: $\{\Upsilon_{\ell:0}, \Upsilon_{\ell+1:1}, \dots, \Upsilon_{k:k-\ell}\}$. With the input of classical shadows, these $k - \ell + 1$ marginals may be simultaneously estimated, leaving the characterisation scaling logarithmic in the number of steps.

Full details of the theorem reconstructing a state from its marginals may be found in Ref. [63], however we reconfigure the statements here in the form of a tensor network diagram in Figure 6. We start with $\Upsilon_{\ell:0}$. Moving one leg across, the next $2\ell + 1$ body marginal is $\text{Tr}_{\sigma_{\ell+1}, \sigma_0}[\Upsilon_{\ell+1:0}]$. However, causality constraints (Equation (9)) mean that this term reduces to $\mathbb{I}_{i_{\ell+1}} \otimes \text{Tr}_{\sigma_0}[\Upsilon_{\ell:0}]$, which is information we already have. Moving one leg over, the next marginal is $\Upsilon_{\ell+1:1}$. This continues until we get to $\Upsilon_{k:k-\ell}$. Collectively, these form the set

$$E := \{\Upsilon_{k:k-\ell}, \mathbb{I}_{i_k} \otimes \text{Tr}_{\sigma_{k-\ell-1}}[\Upsilon_{k-1:k-\ell-1}], \Upsilon_{k-1:k-\ell-1}, \dots, \mathbb{I}_{i_{\ell+1}} \otimes \text{Tr}_{\sigma_0}[\Upsilon_{\ell+1:0}], \Upsilon_{\ell:0}\}. \quad (15)$$

The elements of this set form the local sites in the MPO. The bonds are formed by tracing over the final term of each $\rho \in E$ and taking its pseudoinverse. The connections of these terms to construct the overall MPO is depicted in Figure 6a.

H. Reconstruction statistics

To assess the validity of the MPO model in the main text we determine its ability to make predictions that accurately reflect circuit dynamics. Here, this means predicting the resulting distributions from random sequences of instruments. Consider one such test sequence $\{\mathcal{J}_{20}^{(x_{20})}, \mathcal{J}_{19}^{(x_{19})}, \dots, \mathcal{J}_0^{(x_0)}\}$. Note that the last instrument, \mathcal{J}_{20} , is actually a POVM – an instrument where the post-measurement state is thrown away.

Each instrument is selected by choosing a Haar random unitary to act on the system, and the ancilla qubit measurement outcomes recorded. Because of the characterisation procedure outlined in Appendix E, each in-

strument’s effective map is known, regardless of the local unitary. A single circuit consequently induces a joint probability distribution

$$\Pr(x_{20}, t_{20}; x_{19}, t_{19}; \dots; x_0, t_0 | \mathbf{J}_{20:0}) \quad (16)$$

for the measurement outcomes at the different times. We first sample from this distribution for a given $\mathbf{J}_{20:0}$ by running the sequence on the device at 16 384 shots and recording each of the results. Naturally, at 2×10^6 outcomes, this distribution is already too large to sensibly measure and compare. Hence, we consider marginals of the distribution. A marginal of length ℓ at a leading time j is the marginal distribution of Equation (16)

$$\Pr(x_j, t_j; x_{j-1}, t_{j-1}; \dots; x_{j-\ell+1}, t_{j-\ell+1} | \mathbf{J}_{j:0}). \quad (17)$$

In the main text, we consider up to each contiguous 5-time marginals of a sequence of random instruments, and we sample from the distributions of 170 such random sequences on *ibm_lagos*. The estimate of the MPO representation of $\Upsilon_{20:0}$ can produce a corresponding estimate for the distributions in Equation (17) by computing

$$p_{x_j x_{j-1} \dots x_{j-\ell+1} | \mathbf{J}_{j:0}} = \text{Tr} \left[\left(\mathbb{I}_{t_{20}:t_{j+1}} \otimes \mathcal{J}_j^{(x_j)\text{T}} \otimes \mathcal{J}_{j-1}^{(x_{j-1})\text{T}} \otimes \dots \otimes \mathcal{J}_{j-\ell+1}^{(x_{j-\ell+1})\text{T}} \otimes \mathcal{J}_{j-\ell-2}^{\text{T}} \otimes \dots \otimes \mathcal{J}_0^{\text{T}} \right) \cdot \Upsilon_{20:0} \right], \quad (18)$$

which, for an MPO, can be contracted efficiently. Note that where we have dropped the instrument superscript, this indicates that we have discarded the ancilla outcome, effecting a CPTP map: $\mathcal{J}_i = \mathcal{J}_i^{(0)} + \mathcal{J}_i^{(1)}$. The boxplots of Figure 4c display the Hellinger distance between the quantum computer sample, and Equation (18) for each of the 170 sequences, for each marginal 1 – 5, and for each time 0 – 20.

ACKNOWLEDGMENTS

This work was supported by the University of Melbourne through the establishment of an IBM Quantum

Network Hub at the University. G.A.L.W. is supported by an Australian Government Research Training Program Scholarship. C.D.H. is supported through a Laby Foundation grant at The University of Melbourne. K.M. is supported through Australian Research Council Future Fellowship FT160100073. K.M. and C.D.H. acknowledge the support of Australian Research Council’s Discovery Project DP210100597. K.M. and C.D.H. were recipients of the International Quantum U Tech Accelerator award by the US Air Force Research Laboratory.

-
- [1] R. Horodecki, P. Horodecki, M. Horodecki, and K. Horodecki, *Reviews of Modern Physics* **81**, 865 (2009).
 - [2] B. Lanyon, C. Maier, M. Holzäpfel, T. Baumgratz, C. Hempel, P. Jurcevic, I. Dhand, A. Buyskikh, A. Daley, M. Cramer, *et al.*, *Nature Physics* **13**, 1158 (2017).
 - [3] G. Chiribella, G. M. D’Ariano, and P. Perinotti, *Physical Review Letters* **101**, 180501 (2008).
 - [4] F. A. Pollock, C. Rodríguez-Rosario, T. Frauenheim, M. Paternostro, and K. Modi, *Physical Review A* **97**, 012127 (2018), [arXiv:1512.00589](https://arxiv.org/abs/1512.00589).
 - [5] F. Costa and S. Shrapnel, *New Journal of Physics* **18**, 063032 (2016).
 - [6] F. Costa, M. Ringbauer, M. E. Goggin, A. G. White, and A. Fedrizzi, *Phys. Rev. A* **98**, 012328 (2018).
 - [7] S. Milz and K. Modi, *PRX Quantum* **2**, 030201 (2021), [arXiv:2012.01894](https://arxiv.org/abs/2012.01894).
 - [8] M. M. Wilde, *Quantum Information Theory* (Cambridge University Press, 2013).
 - [9] S. Milz, C. Spee, Z.-P. Xu, F. A. Pollock, K. Modi, and O. Gühne, *SciPost Phys.* **10**, 141 (2021).
 - [10] G. Chiribella, G. M. D’Ariano, P. Perinotti, and B. Valiron, *Phys. Rev. A* **88**, 022318 (2013).

- [11] O. Oreshkov, F. Costa, and Č. Brukner, *Nat. Commun.* **3**, 1092 (2012).
- [12] M. Ringbauer and R. Chaves, *Quantum* **1**, 35 (2017).
- [13] G. Carvacho, F. Andreoli, L. Santodonato, M. Bentinegna, R. Chaves, and F. Sciarrino, *Nat. Commun.* **8**, 14775 (2017).
- [14] S. Milz, F. A. Pollock, T. P. Le, G. Chiribella, and K. Modi, *New J. Phys.* **20**, 033033 (2018).
- [15] M. Ringbauer, F. Costa, M. E. Goggin, A. G. White, and A. Fedrizzi, *npj Quantum Information* **4**, 37 (2018).
- [16] P. Figueroa-Romero, F. A. Pollock, and K. Modi, *Commun. Phys.* (2021).
- [17] G. D. Berk, A. J. P. Garner, B. Yadin, K. Modi, and F. A. Pollock, *Quantum* **5**, 435 (2021).
- [18] G. D. Berk, S. Milz, F. A. Pollock, and K. Modi, *arXiv:2110.02613 [quant-ph]*.
- [19] S. Milz, J. Bavaresco, and G. Chiribella, (2021).
- [20] L. Hardy, *Phil. Trans. R. Soc. A* **370**, 3385 (2012).
- [21] J. Cotler, C.-M. Jian, X.-L. Qi, and F. Wilczek, *J. High Energy Phys.* **2018**, 93 (2018).
- [22] G. A. L. White, C. D. Hill, F. A. Pollock, L. C. L. Hollenberg, and K. Modi, *Nature Communications* **11**, 6301 (2020), *arXiv:2004.14018*.
- [23] G. A. L. White, F. A. Pollock, L. C. L. Hollenberg, K. Modi, and C. D. Hill, (2021), *arXiv:2106.11722*.
- [24] A. Altherr and Y. Yang, *Phys. Rev. Lett.* **127**, 060501 (2021).
- [25] A. Nitzan and M. A. Ratner, *Science* **300**, 1384 (2003).
- [26] K. Sinha, P. Meystre, E. A. Goldschmidt, F. K. Fatemi, S. L. Rolston, and P. Solano, *Phys. Rev. Lett.* **124**, 043603 (2020).
- [27] D. Nagy and P. Domokos, *Phys. Rev. Lett.* **115**, 043601 (2015).
- [28] N. Lambert, Y.-N. Chen, Y.-C. Cheng, C.-M. Li, G.-Y. Chen, and F. Nori, *Nature Physics* **9**, 10 (2013).
- [29] L. P. McGuinness, Y. Yan, A. Stacey, D. A. Simpson, L. T. Hall, D. Maclaurin, S. Prawer, P. Mulvaney, J. Wrachtrup, F. Caruso, R. E. Scholten, and L. C. Hollenberg, *Nature Nanotechnology* **6**, 358 (2011).
- [30] Á. Rivas, S. F. Huelga, and M. B. Plenio, *Reports on Progress in Physics* **77**, 094001 (2014), *arXiv:1405.0303*.
- [31] S. Shrapnel, F. Costa, and G. Milburn, *New Journal of Physics* **20**, 053010 (2018).
- [32] S. Milz, F. Sakuldee, F. A. Pollock, and K. Modi, *Quantum* **4**, 255 (2020), *arXiv:1712.02589*.
- [33] J. Schuff, L. J. Fiderer, and D. Braun, *New Journal of Physics* **22**, 035001 (2020).
- [34] I. A. Aloisio, G. A. L. White, C. D. Hill, and K. Modi, *In preparation* (2022).
- [35] F. A. Pollock, C. Rodríguez-Rosario, T. Frauenheim, M. Paternostro, and K. Modi, *Physical Review Letters* **120**, 040405 (2018), *arXiv:1801.09811*.
- [36] C. Giarmatzi and F. Costa, *Quantum* **5**, 440 (2021).
- [37] Entanglement across indices σ_j , i_j will trivially be large for nearly unitary processes. We care about the entanglement across indices i_j , σ_{j-1} , which measures coherent quantum memory effects between time steps.
- [38] S. T. Flammia, D. Gross, Y.-K. Liu, and J. Eisert, *New Journal of Physics* **14**, 095022 (2012), *arXiv:1205.2300*.
- [39] J. R. West, B. H. Fong, and D. A. Lidar, *Phys. Rev. Lett.* **104**, 130501 (2010).
- [40] C. Guo, K. Modi, and D. Poletti, *Physical Review A* **102**, 062414 (2020).
- [41] K. Goswami, C. Giarmatzi, C. Monterola, S. Shrapnel, J. Romero, and F. Costa, *Phys. Rev. A* **104**, 022432 (2021).
- [42] L. Xiang, Z. Zong, Z. Zhan, Y. Fei, C. Run, Y. Wu, W. Jin, C. Xiao, Z. Jia, P. Duan, J. Wu, Y. Yin, and G. Guo, *arXiv:2105.03333* (2021).
- [43] A. Strathearn, P. Kirton, D. Kilda, J. Keeling, and B. W. Lovett, *Nat. Commun.* **9**, 3322 (2018).
- [44] I. A. Luchnikov, S. V. Vintskevich, H. Ouerdane, and S. N. Filippov, *Phys. Rev. Lett.* **122**, 160401 (2019).
- [45] M. Cygorek, M. Cosacchi, A. Vagov, V. M. Axt, B. W. Lovett, J. Keeling, and E. M. Gauger, *Nature Physics* (2022), [10.1038/s41567-022-01544-9](https://doi.org/10.1038/s41567-022-01544-9).
- [46] H.-Y. Huang, R. Kueng, and J. Preskill, *Nature Physics* **16**, 1050 (2020), *arXiv:2002.08953*.
- [47] S. T. Flammia, (2021), *arXiv:arXiv:2108.05803*.
- [48] M. Heyl, *Reports on Progress in Physics* **81**, 054001 (2018).
- [49] J. J. Hope, G. M. Moy, M. J. Collett, and C. M. Savage, *Phys. Rev. A* **61**, 023603 (2000).
- [50] D. Jaksch and P. Zoller, *Annals of physics* **315**, 52 (2005).
- [51] I. de Vega, D. Porras, and J. Ignacio Cirac, *Phys. Rev. Lett.* **101**, 260404 (2008).
- [52] D. Alonso, S. Brouard, and D. Sokolovski, *Phys. Rev. A* **90**, 032106 (2014).
- [53] F. Caruso, A. W. Chin, A. Datta, S. F. Huelga, and M. B. Plenio, *The Journal of Chemical Physics* **131**, 09B612 (2009).
- [54] H.-Y. Huang, M. Broughton, J. Cotler, S. Chen, J. Li, M. Mohseni, H. Neven, R. Babbush, R. Kueng, J. Preskill, and J. R. McClean, *, 1* (2021), *arXiv:2112.00778*.
- [55] B. Jungnitsch, T. Moroder, and O. Gühne, *Phys. Rev. Lett.* **106**, 190502 (2011).
- [56] G. C. Knee, E. Bolduc, J. Leach, and E. M. Gauger, *Physical Review A* **98**, 062336 (2018), *arXiv:1803.10062*.
- [57] G. Chiribella, G. M. D'Ariano, and P. Perinotti, *Phys. Rev. A* **80**, 022339 (2009).
- [58] M. Malekakhlagh, E. Magesan, and D. C. McKay, *Physical Review A* **102**, 042605 (2020).
- [59] J. Kunjummen, M. C. Tran, D. Carney, and J. M. Taylor, *, 1* (2021), *arXiv:2110.03629*.
- [60] J. Helsen, M. Ioannou, I. Roth, J. Kitzinger, E. Onorati, A. H. Werner, and J. Eisert, *, 1* (2021), *arXiv:2110.13178*.
- [61] S. Milz, F. A. Pollock, and K. Modi, *Open Syst. Inf. Dyn.* **24**, 1740016 (2017).
- [62] G. E. Fux, E. P. Butler, P. R. Eastham, B. W. Lovett, and J. Keeling, *Physical Review Letters* **126**, 200401 (2021).
- [63] T. Baumgratz, D. Gross, M. Cramer, and M. B. Plenio, *Phys. Rev. Lett.* **111**, 020401 (2013).
- [64] D. Henrion and J. Malick, *Optimization Methods and Software* **26**, 23 (2011).
- [65] M. F. Anjos and J. B. Lasserre, *International Series in Operations Research and Management Science*, Vol. 166 (Springer US, 2012) Chap. 20, pp. XI, 960.
- [66] E. Nielsen, K. Rudinger, T. Proctor, A. Russo, K. Young, and R. Blume-Kohout, *Quantum Science and Technology* **5**, 044002 (2020).

APPENDIX

Appendix A: Choi states

1. Quantum channels

The Choi representation of quantum channels used in the main text is defined as follows. The Choi-Jamiolkowski isomorphism (CJI) is the correspondence between mappings of bounded linear operators, $\mathcal{B}(\mathcal{H}_{\text{in}}) \rightarrow \mathcal{B}(\mathcal{H}_{\text{out}})$ and bipartite quantum states on the respective spaces, $\mathcal{B}(\mathcal{H}_{\text{out}}) \otimes \mathcal{B}(\mathcal{H}_{\text{in}})$. Explicitly, the Choi state $\hat{\mathcal{E}}$ of some channel \mathcal{E} on a d -dimensional system is formed by the action of \mathcal{E} on one half of an unnormalised maximally entangled state $|\Phi^+\rangle = \sum_{i=1}^d |ii\rangle$:

$$\hat{\mathcal{E}} := (\mathcal{E} \otimes \mathcal{I}) [|\Phi^+\rangle\langle\Phi^+|] = \sum_{i,j=1}^d \mathcal{E}[|i\rangle\langle j|] \otimes |i\rangle\langle j|, \quad (\text{A1})$$

where \mathcal{I} is the identity map. This is depicted in Figure 7a. The action of \mathcal{E} on some input state ρ_{in} is then given in terms of its Choi state by the projection

$$\mathcal{E}[\rho_{\text{in}}] = \text{Tr}_{\text{in}} \left[(\mathbb{I}_{\text{out}} \otimes \rho_{\text{in}}^{\text{T}}) \hat{\mathcal{E}} \right]. \quad (\text{A2})$$

Quantum channels can be partitioned into three physically distinct vector spaces: linear combinations of unitary operators; maps which un-mix the identity; and stochastic maps which reduce the trace of a state. Although we employ the Choi form for most computations in this work, the most straightforward way to see these categories is with the Pauli transfer matrix (PTM) representation $R_{\mathcal{E}}$. Each matrix element is given by the action of \mathcal{E} on a full basis of Pauli operators $P \in \{\mathbb{I}, X, Y, Z\}$:

$$(R_{\mathcal{E}})_{ij} = \text{Tr}[P_i \mathcal{E}[P_j]]. \quad (\text{A3})$$

For a channel \mathcal{E} to be trace-preserving, we must have $\text{Tr}[\mathcal{E}[\rho]] = \text{Tr}[\rho] \forall \rho$. In PTM form, since $\text{Tr}[P_j] = \delta_{0j}$, then $\text{Tr}[\mathcal{E}[P_j]] = \delta_{0j}$. This implies that $(R_{\mathcal{E}})_{0j} = \delta_{0j}$ for trace preservation. Similarly, since unitality demands that $\mathcal{E}[\mathbb{I}] = \mathbb{I}$, then $(R_{\mathcal{E}})_{i0} = \text{Tr}[P_i \mathcal{E}[\mathbb{I}]] = \text{Tr}[P_i \mathbb{I}] = \delta_{i0}$. The remaining operations are linear combinations of unitary maps.

Note that in comparing Equations (A3) and (A2), the elements of the PTM are simply the Pauli expectation coefficients of the Choi matrix, up to transpose of the Y operator. i.e.

$$(R_{\mathcal{E}})_{ij} = \text{Tr} \left[P_i \otimes P_j^{\text{T}} \hat{\mathcal{E}} \right], \quad (\text{A4})$$

this is depicted in Figure 1b of the main text. We emphasise these properties of quantum channels as properties that need to be tracked both in imposing the unitary restriction to tomographically incomplete data, and in creating complete bases with optimally separated trace-decreasing and non-unital components.

2. Process tensors

Process tensors can be seen as a formal generalisation of quantum channels to multi-time processes. To be precise, we consider the situation where a k -step process is driven by a sequence $\mathbf{A}_{k-1:0}$ of control operations, each represented mathematically by CP maps: $\mathbf{A}_{k-1:0} := \{\mathcal{A}_0, \mathcal{A}_1, \dots, \mathcal{A}_{k-1}\}$, after which we obtain a final state $\rho_k(\mathbf{A}_{k-1:0})$ conditioned on this choice of interventions. These controlled dynamics have the form:

$$\rho_k(\mathbf{A}_{k-1:0}) = \text{tr}_E[U_{k:k-1} \mathcal{A}_{k-1} \cdots U_{1:0} \mathcal{A}_0(\rho_0^{SE})], \quad (\text{A5})$$

where $U_{k:k-1}(\cdot) = u_{k:k-1}(\cdot)u_{k:k-1}^{\dagger}$. Eq. (A5) can be used to define a mapping from past controls $\mathbf{A}_{k-1:0}$ to future states $\rho_k(\mathbf{A}_{k-1:0})$, which is the process tensor $\mathcal{T}_{k:0}$:

$$\mathcal{T}_{k:0}[\mathbf{A}_{k-1:0}] = \rho_k(\mathbf{A}_{k-1:0}). \quad (\text{A6})$$

A generalisation of the CJI allows this mapping to be represented as a many-body quantum state. The circuit view of this CJI is depicted in Figure 7b. In this picture, at each time, one half of a fresh Bell pair is swapped to

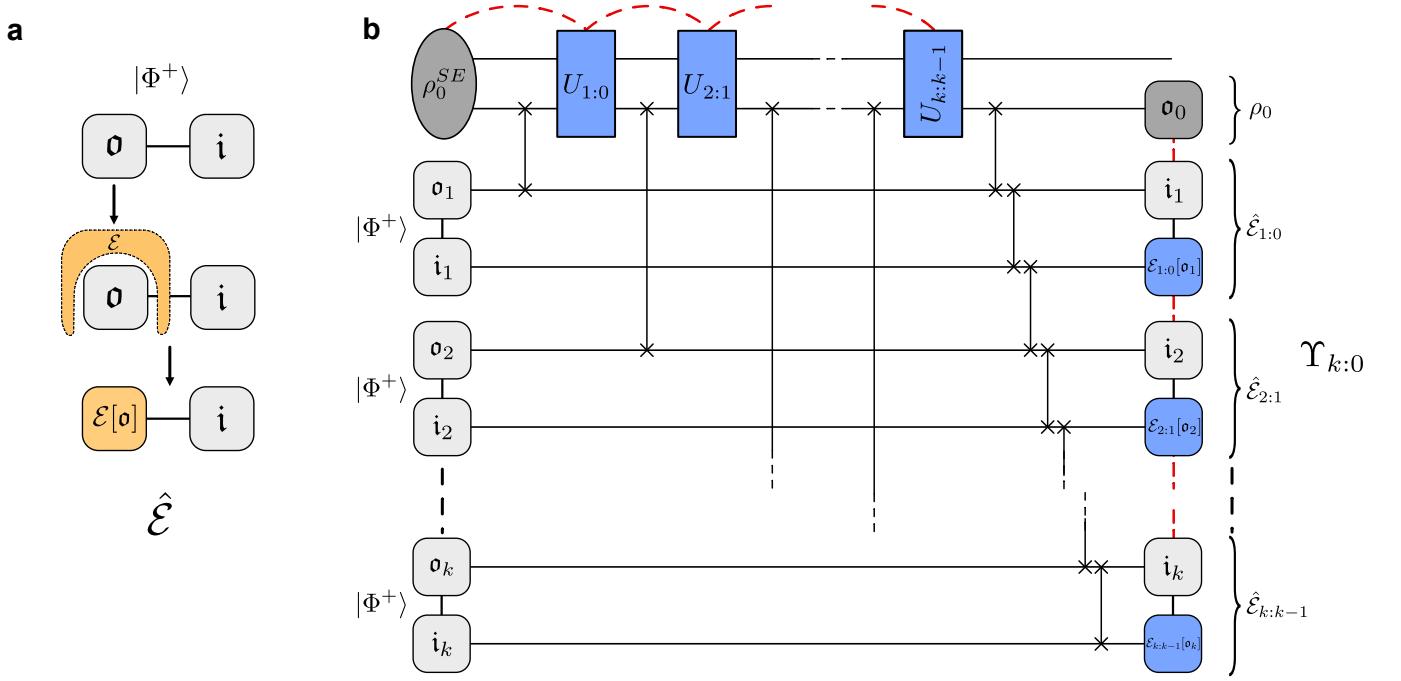


FIG. 7. Circuit diagrams of the conventional and generalised Choi-Jamiolkowski isomorphism. **a** Two-time processes are represented by quantum channels; their Choi state is given by the channel acting on one half of a Bell pair. **b** Multi-time processes are represented by process tensors; their Choi state is given for a k -step process by swapping in one half of k Bell pairs at different times. The non-Markovian correlations are mapped onto spatial correlations in the Choi state. The marginals of the process tensor are quantum channels, as well as the average initial state.

interact with the environment. The mixed state at the end, $\Upsilon_{k:0}$ is the process tensor Choi state. This can be used to produce the action of the process tensor on any controlled sequence of operations (consistent with the time steps) by projection:

$$\rho_k(\mathbf{A}_{k-1:0}) = \text{Tr}_{\bar{o}_k} \left[\Upsilon_{k:0} (\mathbb{I}_{o_k} \otimes \mathcal{A}_{k-1} \otimes \cdots \otimes \mathcal{A}_0)^T \right], \quad (\text{A7})$$

where \bar{o}_k is every index except o_k . This equation is inclusive of all intermediate SE dynamics as well as any initial correlations, and illustrates how sequences of operations constitute observables of the process tensor.

Each time has an associated output (o) and input (i) leg from the process. If the dynamical process is non-Markovian, then the system-environment interactions will distribute temporal correlations as spatial correlations between different legs of the process tensor. These correlations may then be probed using any number of established quantum or classical many body tools. In Figure 7b we have depicted these correlations in red. Correlations between consecutive i/o legs (presented in black) are expected to be very high for nearly-unitary processes, and do not constitute a measure of non-Markovianity. In this vein, it can be shown that a process is Markovian if and only if it can be expressed in the form [35]:

$$\Upsilon_{k:0}^{(\text{Markov})} = \hat{\mathcal{E}}_{k:k-1} \otimes \hat{\mathcal{E}}_{k-1:k-2} \otimes \cdots \otimes \hat{\mathcal{E}}_{1:0} \otimes \rho_0. \quad (\text{A8})$$

Appendix B: Temporal entanglement for quantum sensing

We outline here the simulations conducted to produce the results of Figures 2c and 2d. We consider a simple spin-spin Hamiltonian $\mathcal{H} = \mathcal{H}_S \otimes \mathcal{H}_E$ in the rotating frame of the sensor. This takes the form:

$$\mathcal{H} = \omega_L \sigma_z^{(E)} + \mathcal{H}_I, \quad (\text{B1})$$

where ω_L is the Larmor frequency of the environment spin – we take this to be a nuclear spin of 1.85×10^6 Hz); $\sigma_Z^{(E)} \in \mathcal{B}(\mathcal{H}_E)$ is an operator on the nuclear spin (dropping the system identity for simplicity); and \mathcal{H}_I is the interaction Hamiltonian.

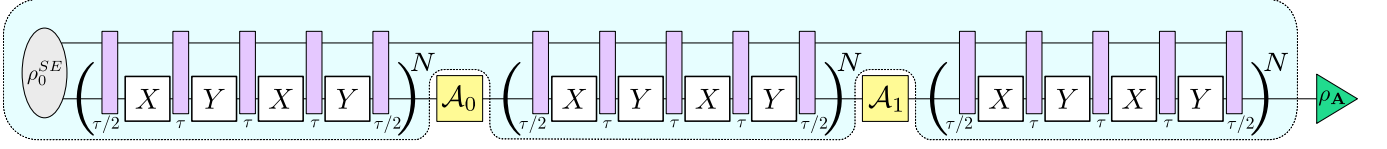


FIG. 8. A circuit diagram showing a process tensor built around a DD sequence. When on resonance, the DD sequence amplifies interactions with the environment. The process tensor can then be used to detect and characterise the temporal correlations generated.

A straightforward quantum sensing protocol is to apply dynamical decoupling (DD) sequences (we choose XY4) to the central spin, and sweep across a range of frequencies. The spin is first placed in the $|i+\rangle$ eigenstate with a $R_x(\pi/2)$ rotation, a DD sequence applied, and then $R_x(-\pi/2)$ followed by measurement of the ground state population. This is the coherence curve presented in the main text, Figures 2c and 2d.

By inserting some probe operations within the filter sequence as per Figure 8, we can also spectroscopically determine non-Markovianity when the sequence locks onto these frequencies. We propose the reconstruction of a restricted process tensor around the DD sequence. The use of our unitary temporal entanglement witnesses, can determine whether the interaction is genuinely quantum or not.

For the examples of classical and quantum interactions given in the main text (Figures 2c and 2d), we choose interactions:

$$\begin{aligned}\mathcal{H}_I^{(\text{Classical})} &= g \cdot \sigma_y \otimes \sigma_z \\ \mathcal{H}_I^{(\text{Quantum})} &= \frac{g}{2}(\sigma_z + \sigma_x) \otimes (\sigma_z + \sigma_y)\end{aligned}\quad (\text{B2})$$

The interaction $\mathcal{H}_I^{(\text{Classical})}$ generates no entanglement in the process tensor because it is a two-qubit commuting Hamiltonian, meaning that it can be locally diagonalised [34]. Thus, after tracing over the environment, the interaction is locally equivalent to a stochastic mixture of Z -rotations, which is non-Markovian but separable. It could hence be replaced with a classical source of correlated randomness, such as a fluctuating magnetic field. Meanwhile, as verified by the entanglement witness (and the negativity of the process tensor), $\mathcal{H}_I^{(\text{Quantum})}$ generates quantum correlations in time, which could only be created by a genuinely quantum environment.

Appendix C: Exploring process tensor families

The set of physical process tensors is convex and exists as the intersection of positive semi-definite (PSD) matrices with the affine space generated by the collection of causality conditions, $\text{Tr}_{\sigma_j}[\Upsilon_{j:0}] = \mathbb{I}_{i_j} \otimes \Upsilon_{j-1:0} \forall j \in \{1 : k\}$. These causality conditions may be better understood in the context of a density operator as setting expectation values of non-trivially chosen Pauli operators to zero, as outlined in our accompanying Article [23]. There, we use the `pgdB` algorithm to best fit experimental process tensor data. This minimises a log-likelihood cost function through gradient descent, where at each step a projection is made such that the optimisation direction is physical. We employ our own projection method which is suited to the large matrices used in process tensor analysis.

Since the causality constraints take the same form as basis measurements of the process tensor (linear inhomogeneous equations), here, we extend this method to allow for straightforward optimisation of arbitrary objective functions over the spaces of processes consistent with limited experimental data. With $\Upsilon_{k:0} = \Upsilon_{k:0}^{(R)} + \Upsilon_{k:0}^{(R_\perp)}$ the decomposition of a process tensor into the experimentally observed restricted process tensor, $\Upsilon_{k:0}^{(R)}$, and its orthogonal complement, let $\Upsilon_{k:0}^{(R)}$ be constructed through the final-state measurement conditioned on a set of basis sequences $\{\mathbf{B}_{k-1:0}^{\vec{\mu}}\} = \{\otimes_{i=0}^{k-1} \mathcal{B}_i^{\mu_j}\}_{\vec{\mu}=(1,1,\dots,1)}^{(d^1, d^2, \dots, d^k)}$. Although this object has well-defined properties – such as its action on the span of its basis elements – one cannot use it to directly estimate correlations in $\Upsilon_{k:0}$. For each sequence, and each measurement outcome, we have a set of equations

$$\text{Tr} \left[\Upsilon_{k:0} \left(\Pi_i \otimes \mathbf{B}_{k-1:0}^{\vec{\mu}T} \right) \right] = p_{i,\vec{\mu}}, \quad (\text{C1})$$

which we choose to impose in our exploration of the process tensor family. To fix these, we append the expectation of each basis sequence $\Pi_i \otimes \mathbf{B}_{k-1:0}^{\vec{\mu}}$ with its corresponding observed probability $p_{i,\vec{\mu}}$ which describes the affine space.

That is, imposing the matrix-vector equation

$$\begin{pmatrix} \langle\langle \mathcal{P}_0 | \\ \langle\langle \mathcal{P}_1 | \\ \vdots \\ \langle\langle \mathcal{P}_N | \\ \langle\langle \mathbb{I} | \\ \langle\langle \Pi_{i_0} \otimes \mathbf{B}_{k-1:0}^{\vec{\mu}_0} | \\ \langle\langle \Pi_{i_0} \otimes \mathbf{B}_{k-1:0}^{\vec{\mu}_1} | \\ \vdots \\ \langle\langle \Pi_{i_L} \otimes \mathbf{B}_{k-1:0}^{\vec{\mu}_N} | \end{pmatrix} \cdot |\Upsilon_{k:0}\rangle\rangle = \begin{pmatrix} 0 \\ 0 \\ \vdots \\ 0 \\ 1 \\ p_{i_0, \vec{\mu}_0} \\ p_{i_0, \vec{\mu}_1} \\ \vdots \\ p_{i_L, \vec{\mu}_N} \end{pmatrix}, \quad (\text{C2})$$

where $|\cdot\rangle\rangle$ is the row-vectorisation of an operator, and $\langle\langle \cdot |$ its complex conjugate. Each \mathcal{P}_i here is an n -qubit Pauli operator whose expectation needs to be zero for causality to follow. It is important that the observed constraints come from a procedure that guarantees the feasibility of the problem, such as a maximum likelihood estimation first. If experimental data are directly used as the set of observed probabilities, there may not exist a positive operator consistent with that data – i.e. the intersection between the affine space and PSD matrices may be empty.

Full details and benchmarking of the `pgdb` algorithm for QPT can be found in Ref. [56]. Here, we provide the pseudocode in this context, which forms the basis for our bounding of process tensor quantities.

Algorithm 1 `pgdb`

```

1:  $j = 0, n = d_S^{2k+1}$ 
2: Initial estimate:  $\Upsilon_{k:0}^{(0)} = \Upsilon_{k:0}^{(\text{MLE})}$ 
3: Set metaparameters:  $\alpha = 2n^2/3, \gamma = 0.3, \mu = 1 \times 10^{-3}$ 
4: while  $f(\Upsilon_{k:0}^{(j)}) - f(\Upsilon_{k:0}^{(n+1)}) > 1 \times 10^{-6}$  do
5:    $D^{(j)} = \text{Proj}_{S_n^+ \cap \mathcal{V}}(\Upsilon_{k:0}^{(j)} - \mu \nabla f(\Upsilon_{k:0}^{(j)})) - \Upsilon_{k:0}^{(j)}$ 
6:    $\beta = 1$ 
7:   while  $f(\Upsilon_{k:0}^{(j)} + \beta D^{(j)}) > f(\Upsilon_{k:0}^{(j)}) + \gamma \beta \langle\langle D^{(j)}, \nabla f(\Upsilon_{k:0}^{(j)}) \rangle\rangle$  do
8:      $\beta = 0.5\beta$ 
9:   end while
10:   $\Upsilon_{k:0}^{(j+1)} = \Upsilon_{k:0}^{(j)} + \beta D^{(j)}$ 
11:   $j = j + 1$ 
12: end while
13: return  $\Upsilon_{k:0}^{(\text{est})} = \Upsilon_{k:0}^{(j+1)}$ 

```

In particular, the objective function f is chosen to be information-theoretic quantities stated in the main text (QMI, fidelity, purity, negativity), and ∇f their analytic gradients. Extremisation of these objective functions is consequently found through projected gradient descent (or ascent), with positivity and the affine constraints (C2) satisfied at each step. Algorithmic performance of the projection subroutine is contingent on the condition number of the constraint matrix. For this reason, it is important to cast the problem not necessarily in terms of the Choi states of the experimental operations, but ideally in terms of a mutually unbiased basis that spans the same space. In our case, with unitary-only control, these were the weight-2 Pauli operators on $\mathcal{B}(\mathcal{H}_{\text{out}}) \otimes \mathcal{B}(\mathcal{H}_{\text{in}})$. Full details of the projection subroutine

$$\text{Proj}_{S_n^+ \cap \mathcal{V}}(v_0) = \underset{v \in S_n^+ \cap \mathcal{V}}{\text{argmin}} \|v - v_0\|^2 \quad (\text{C3})$$

can be found in Refs. [23, 64, 65]. In short, let $|\Upsilon_{k:0}\rangle\rangle := v_0$, let $\kappa \in \mathbb{R}^m$ for m affine constraints, and let the terms in Equation (C2) be denoted $A \cdot v = b$. Diagonalising $\Upsilon_{k:0}$ gives $\Upsilon_{k:0} = UDU^\dagger$ where $D = \text{diag}(\lambda_1, \lambda_2, \dots, \lambda_n)$ is real. Then the projection onto S_n^+ is:

$$\text{Proj}_{S_n^+}(\Upsilon) = U \text{diag}(\lambda_0^+, \dots, \lambda_n^+) U^\dagger \quad (\text{C4})$$

with $\lambda_j^+ := \max\{\lambda_j, 0\}$. Now, defining $v(\kappa) := \text{Proj}_{S_n^+}(v_0 + A^\dagger \kappa)$ (note that projection of a vector here carries implied matrix reshape, positive projection, followed by vector reshape), it can be shown that the unconstrained minimisation of the function

$$\theta(\kappa) = -\|v(\kappa)\|^2 + b^\dagger \kappa, \quad (\text{C5})$$

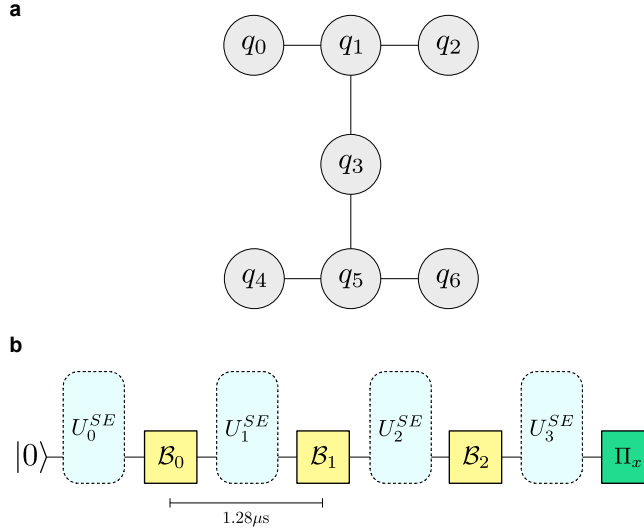


FIG. 9. **a** Qubit map of *ibmq_casablanca*, q_5 was the system qubit in all experiments. **b** Structure of the process tensor circuits for this device: a three-step process tensor constitutes three basis operations, followed by measurement. For all six experiments, we fixed the wait time at $1.28 \mu\text{s}$ and varied the background.

whose gradient is

$$\nabla\theta(\kappa) = -Av(\kappa) + b, \quad (\text{C6})$$

is the unique solution to Equation (C3). For our purposes then, we employ the L-BFGS algorithm to minimise $\theta(\kappa)$, and thus project some v_0 onto $\mathcal{S}_n^+ \cap \mathcal{V}$.

Appendix D: Overview of experiments

Here, we discuss the details of the IBM Quantum experiments conducted in the main text. The four devices used were *ibmq_cairo* (27 qubits, QV64), *ibmq_auckland* (27 qubits, QV64), *ibmq_casablanca* (7 qubits, QV32), and *ibmq_perth* (7 qubits, QV32).

In Table I we characterise the noise on *ibmq_casablanca*. The layout of this device is shown in Fig 9a and the structure of the process tensor experiments in Fig 9b. q_5 was used as the system qubit for all experiments shown in Table I of the main text, and had a measured T_2 time of $123.65 \mu\text{s}$ during the period over which data was collected. For experiments #1–#6 the backgrounds were varied, and the wait time between each time step identically fixed to $1.28 \mu\text{s}$. A ten-unitary basis was used, for a total of 3000 circuits per experiment at 4096 shots. The details of each background are as follows:

1. No control operations on any other qubits.
2. q_3 , q_4 , and q_6 were each initialised into a $|+\rangle$ state at the beginning of the circuits and left idle.
3. q_3 , q_4 , and q_6 were each initialised into a $|+\rangle$ state at the beginning of the circuits, and, in each wait period, four sequential CNOTs controlled by q_3 and with q_1 as a target were implemented.
4. q_3 , q_4 , and q_6 were all dynamically decoupled using the QDD scheme with an inner loop of 2 Y gates and an outer loop of 2 X gates. i.e. a sequence $Y-Y-X-Y-Y-X-Y-Y$.
5. q_0 , q_1 , and q_2 were initialised into a $|+\rangle$ state and left idle.
6. q_3 was initialised into a $|+\rangle$ state, followed by a wait time of 320 ns, and then q_1 also initialised into a $|+\rangle$ state and left idle.

To account for the effects of measurement errors on all process tensor estimates, we first performed gate set tomography (GST) on the system qubit using the `pyGSTi` package [66]. This was used to obtain a high quality estimate of the

POVM $\{|+\rangle\langle+|, |-\rangle\langle-|, |i+\rangle\langle i+|, |i-\rangle\langle i-|, |0\rangle\langle 0|, |1\rangle\langle 1|\}$, which was then used in the maximum likelihood estimate of each process tensor.

In Figure 4b, we look at some of the macro properties of correlated noise occurring on *ibm_perth*. This has the same physical layout as *ibmq_casablanca*, shown in Figure 9. On this device, q_3 was chosen as the system qubit, and q_5 the ancilla for implementation of instruments, since these two qubits had the shortest CNOT gate time. In the background process, we applied two random elements of $SU(4)$ between pairs $q_0 - q_1$ and $q_1 - q_2$, compiled down to the native gates of the device. The idle time on the system qubit per step was around $1.8 \mu s$ as a result.

Appendix E: Designing a basis of quantum instruments

The extra control needed for tomographically complete observation of a process tensor are non-unital maps and trace-decreasing. As discussed in Section A 1 and depicted in Figure 1b, these are the remaining quantum operations that have Choi states with non-trivial local expectation values. In particular, the respective characteristic features of these are:

$$\begin{aligned} \mathcal{E}_{\text{NU}}[\mathbb{I}] &\neq \mathbb{I} \\ \text{Tr}_{\text{out}}[\hat{\mathcal{E}}_{\text{TD}}] &\prec \mathbb{I}. \end{aligned} \tag{E1}$$

That is, non-unitals map the maximally mixed state elsewhere, and trace-decreasing maps are non-deterministic. For a qubit with 16 superoperator dimensions, these classes of maps occupy three dimensions each: unmixing in X, Y and Z directions, and projecting in X, Y and Z directions.

In an idealised setting, a complete operator basis can be implemented by measuring the system with an informationally complete POVM, followed by independent fresh preparation of a state from an informationally complete set. However, in practical terms, this set of operations suffers at this stage from being too noisy, invasive, and over a time frame which is long in comparison to possible SE dynamics. As an alternative, we leverage the use of an ancilla qubit and drive a short entangling interaction, followed by projective measurements on the ancilla. This generates an effective map on the system which can be partially controlled through a local unitary operation. The system-ancilla circuit we design uses the native cross-resonance interaction as well as local operations to achieve large values for each $(R_{\mathcal{E}})_{i_0}$ and $(R_{\mathcal{E}})_{0_j}$ such that a well-conditioned basis may be designed.

In PTT, it is necessary that the instruments be well-characterised. To achieve this, we design a process tensor whose mapping is from the local pulse parameters to the effective operation on the system. The idealisation of this is as follows. An ancilla qubit is prepared in the state $(|0\rangle + i|1\rangle)/\sqrt{2}$, meanwhile the system is prepared in one of the four states $\{|+\rangle\langle+|, |i+\rangle\langle i+|, |0\rangle\langle 0|, |1\rangle\langle 1|\}$. We then drive the interaction $R_{XZ}(\gamma) := \exp(-\frac{i\gamma}{2} X_A \otimes Z_S)$ – which is the native cross-resonance interaction on IBM Quantum devices – for some γ . An S gate is then applied to the ancilla, followed by a unitary on the system parametrised as

$$U(\theta, \phi, \lambda) = \begin{pmatrix} \cos(\theta/2) & -e^{i\lambda} \sin(\theta/2) \\ e^{i\phi} \sin(\theta/2) & e^{i\lambda+i\phi} \cos(\theta/2) \end{pmatrix}. \tag{E2}$$

A second $U_{XZ}(\gamma)$ chirp is then applied, followed by projective Z measurement on the ancilla as well as QST on the system. The outcome of the ancilla measurement $|x\rangle\langle x|$ is then attached to the reconstructed state. The end result is a parametrised quantum instrument on the system $\Lambda_x(\theta, \phi, \lambda)$. The circuit presented is designed such that a set of parameter values exists to amplify each of the six (three non-unital and three trace-decreasing) EB directions. The theoretical matrix elements corresponding to a $|0\rangle\langle 0|$ measurement on the ancilla, with $\gamma = \pi/4$ are:

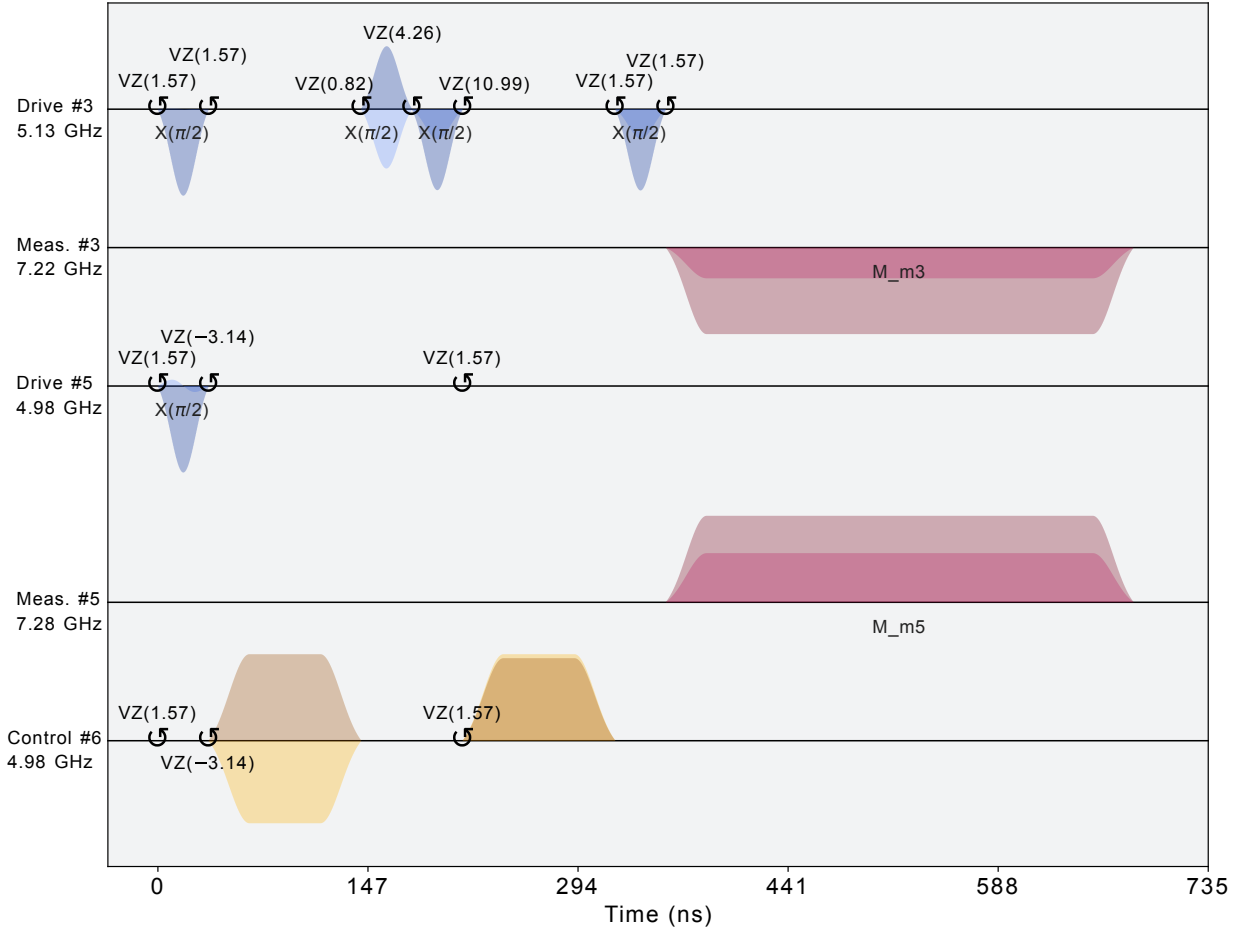


FIG. 10. Sample pulse schedule for instrument creation on *ibm_perth*. We manually drive short Gaussian square cross-resonance pulses between the system qubit and the ancilla qubit. The local system operations – depicted through a series of physical pulses and frame shifts on drive channel 3 – constitute the restricted process tensor used for instrument creation.

$$\begin{aligned}
(R_{\Lambda_0})_{x0} &= \frac{\sqrt{2}}{2} \cos \phi \sin \theta - 2 \cos \frac{\theta}{4} \sin^3 \frac{\theta}{4} \sin \phi, \\
(R_{\Lambda_0})_{y0} &= \frac{1}{4} \cos \phi \left(2 \sin \frac{\theta}{2} - \sin \theta \right) + \frac{\sqrt{2}}{2} \sin \theta \sin \phi, \\
(R_{\Lambda_0})_{z0} &= \frac{1}{8} (-1 + 5 \cos \theta), \\
(R_{\Lambda_0})_{0x} &= \sin \frac{\theta}{2} \left(\sqrt{2} \cos \lambda \sin^2 \frac{\theta}{4} + \cos^2 \frac{\theta}{4} \sin \lambda \right), \\
(R_{\Lambda_0})_{0y} &= \frac{1}{2} \sin \frac{\theta}{2} \left[\left(1 + \cos \frac{\theta}{2} \right) \cos \lambda - \sqrt{2} \left(1 - \cos \frac{\theta}{2} \right) \sin \lambda \right], \\
(R_{\Lambda_0})_{0z} &= \frac{1}{8} (3 + \cos \theta).
\end{aligned} \tag{E3}$$

This suffices for a complete basis. When implemented in practice, however, this instrument will be noisy: the cross-resonance interaction is imperfect and generates additional local terms in the Hamiltonian as well as slight decoherence. Moreover, the measurements themselves made on each qubit have some associated error. These issues may be well accounted-for as long as the instrument is characterised. However, employing QPT will only be valid for a single set of local parameter values – and it would be highly expensive to repeat the procedure for every desired local gate. Instead, we perform restricted PTT with a basis of unitary operations on the system for an informationally complete set of measurements. This requires 40 circuits. Let the resulting two-step process tensor be denoted by Υ_I .

Note that this process tensor maps to the two-qubit SA output which corresponds to the classical state $|x\rangle\langle x|$ on A and the quantum state $\rho^{(x)}$ on S . Let $\hat{\mathcal{P}}_i$ be the Choi state of the preparation operations $\{H, SH, \mathbb{I}, X\}$, and finally, let $\hat{\mathcal{U}}(\theta, \phi, \lambda)$ be the Choi state of the local unitary. The Choi state of the parametrised instrument corresponding to outcome x can be written as

$$\Lambda_x(\theta, \phi, \lambda) = \sum_{i=0}^3 \rho_i'^{(x)}(\theta, \phi, \lambda) \otimes \omega_i^T, \quad (\text{E4})$$

where each $\rho_i'^{(x)}(\theta, \phi, \lambda)$ is the output state on the system level subject to some choice of local parameter values. Now, since Υ_I maps from these two local operations, we have

$$\text{Tr}_{\text{in}} \left[\Upsilon_I \cdot (\mathbb{I}_S \otimes \hat{\mathcal{U}}(\theta, \phi, \lambda)^T \otimes \hat{\mathcal{P}}_i^T) \right] = |0\rangle\langle 0| \otimes \rho_i'^{(0)}(\theta, \phi, \lambda) + |1\rangle\langle 1| \otimes \rho_i'^{(1)}(\theta, \phi, \lambda). \quad (\text{E5})$$

This allows us to re-write Equation (E4) in terms of our reconstructed process tensor:

$$\Lambda_x(\theta, \phi, \lambda) = \sum_{i=0}^3 \text{Tr}_{\text{in}, A} \left[\Upsilon_I \cdot \left(|x\rangle\langle x| \otimes \mathbb{I}_S \otimes \hat{\mathcal{U}}(\theta, \phi, \lambda)^T \otimes \hat{\mathcal{P}}_i^T \right) \right] \otimes \omega_i^T \quad (\text{E6})$$

This outline is the idealised version of the procedure. In reality, we first perform GST to obtain estimates of both the system input states ρ_i and the system and ancilla POVMs. This ensures that the resulting PTT to estimate Υ_I and QPT on the instrument is self-consistent. Using Equation (E6) we then have an accurate representation of the effective instrument acting on the system for any choice of θ , ϕ , and λ . Finally, noting that we may reset the ancilla qubit after each projective measurement to reuse it, this permits us the necessary control for tomographically complete observation of a multitime process.